



1 **Radiocarbon in atmospheric CH<sub>4</sub> and CO<sub>2</sub> at Jungfraujoch in  
2 2019-2024: influence of regional nuclear emissions and current  
3 global atmospheric <sup>14</sup>CH<sub>4</sub> signal**

4

5 Thomas Laemmel<sup>1,2</sup>, Dylan Geissbühler<sup>1,2</sup>§, Stephan Henne<sup>3</sup>, Ryo Fujita<sup>4</sup>, Heather Graven<sup>5</sup>,  
6 Christophe Espic<sup>1,2,\*</sup>, Matthias Bantle<sup>1</sup>, Negar Haghipour<sup>6</sup>, Franz Conen<sup>7</sup>, Dominik Brunner<sup>3</sup>,  
7 Martin Steinbacher<sup>3</sup>, Giulia Zazzeri<sup>8</sup>, Samuel Hammer<sup>9</sup>, Markus Leuenberger<sup>2,10</sup>, Sönke  
8 Szidat<sup>1,2</sup>

9

10 <sup>1</sup>Department of Chemistry, Biochemistry and Pharmaceutical Sciences, University of Bern, Bern, Switzerland

11 <sup>2</sup>Oeschger Centre for Climate Change Research, University of Bern, Bern, Switzerland

12 <sup>3</sup>Empa, Swiss Federal Laboratories for Materials Science and Technology, Dübendorf, Switzerland

13 <sup>4</sup>Meteorological Research Institute, Japan Meteorological Agency, Tsukuba, Japan

14 <sup>5</sup>Department of Physics, Imperial College London, London, United Kingdom

15 <sup>6</sup>Department of Earth and Planetary Sciences and Laboratory of Ion Beam Physics, ETH Zurich, Zurich,  
16 Switzerland

17 <sup>7</sup>Department of Environmental Sciences, University of Basel, Basel, Switzerland

18 <sup>8</sup>Ricerca sul Sistema Energetico – RSE S.p.A., Milan, Italy

19 <sup>9</sup>Institute of Environmental Physics, Heidelberg University, ICOS-CRL, Heidelberg, Germany

20 <sup>10</sup>Climate and Environmental Physics, University of Bern, Bern, Switzerland

21 §now: Institute for Marine and Atmospheric Research Utrecht, Utrecht University, Utrecht, The Netherlands

22 \*now: MIRO Analytical AG, Wallisellen, Switzerland

23

24 *Correspondence to:* Thomas Laemmel (tlaemmel@gmail.com)

25



26 **Abstract.** Radiocarbon ( $^{14}\text{C}$ ) is a valuable tracer to determine the relative fossil fractions of emitted carbonaceous  
27 greenhouse gases, such as  $\text{CO}_2$  and  $\text{CH}_4$ . While atmospheric  $\Delta^{14}\text{CO}_2$  measurements have been conducted at  
28 multiple sites for several decades,  $\Delta^{14}\text{CH}_4$  measurements remain more limited, mainly due to measurement  
29 challenges. In addition, nuclear power plant  $^{14}\text{CH}_4$  emissions can complicate data interpretation. In this study,  
30 biweekly  $\Delta^{14}\text{CH}_4$  and  $\Delta^{14}\text{CO}_2$  measurements at the Swiss High-Altitude Research Station Jungfraujoch (JFJ, about  
31 3500 m a.s.l.) between 2019 and 2024 are presented. Over this period,  $\Delta^{14}\text{CH}_4$  values showed an increase from  
32  $350 \pm 19 \text{ ‰}$  to  $381 \pm 13 \text{ ‰}$ , while  $\Delta^{14}\text{CO}_2$  values decreased from  $-2.0 \pm 3.8 \text{ ‰}$  to  $-12.7 \pm 2.0 \text{ ‰}$ , respectively. The  
33 former is related to the slight increase of  $^{14}\text{CH}_4$  emissions from the nuclear industry over the last years, while the  
34 latter is linked to the dilution of the  $^{14}\text{CO}_2$  signal due to the release of  $^{14}\text{C}$ -devoid  $\text{CO}_2$  from combustion of fossil  
35 fuels. Despite its high elevation, JFJ is still influenced by nuclear power plants (NPPs) operating in Europe.  
36 Considering a European-scale atmospheric dispersion model and  $^{14}\text{CH}_4$  and  $^{14}\text{CO}_2$  emissions from European NPPs,  
37 the mean nuclear  $^{14}\text{C}$  contribution to our individual measurements was estimated to be  $7 \pm 9 \text{ ‰}$  for  $\Delta^{14}\text{CH}_4$  and  
38  $0.2 \pm 0.4 \text{ ‰}$  for  $\Delta^{14}\text{CO}_2$ . Furthermore, our  $\Delta^{14}\text{CH}_4$  measurements reasonably agree with simulated atmospheric  
39 values of  $\Delta^{14}\text{CH}_4$  estimated by a global atmospheric one-box model and an estimation of global nuclear  $^{14}\text{CH}_4$   
40 emissions.

41



42 1. Introduction

43 Carbon dioxide (CO<sub>2</sub>) and methane (CH<sub>4</sub>) are the two main anthropogenic greenhouse gases (GHGs) responsible  
44 for global climate change (IPCC, 2023; WMO, 2025). Since the Industrial Revolution around 1850, their global  
45 atmospheric concentrations have been multiplied by about 1.5 and 2.7, respectively, from around 285 to 422.8 ppm  
46 in 2024 for CO<sub>2</sub> (Etheridge et al., 1996; Lan et al., 2025b) and from around 800 to 1930 ppb in 2024 for CH<sub>4</sub>  
47 (Hmiel et al., 2020; Lan et al., 2025a). Anthropogenic emissions of CO<sub>2</sub> and CH<sub>4</sub> (mainly from the energy sector  
48 for fossil CO<sub>2</sub> and CH<sub>4</sub>, and agriculture and waste management for biogenic CH<sub>4</sub>) are responsible for this rise in  
49 concentrations and resulting climate change. In the period 2010-2019, CO<sub>2</sub> and CH<sub>4</sub> were responsible for a global  
50 warming of around 0.8°C and 0.5°C, respectively, relative to the period 1850-1900 (IPCC, 2023). To implement  
51 effective mitigation measures, the main emission sources of both GHGs have to be better quantified and monitored.

52 Radiocarbon (<sup>14</sup>C), a radioactive isotope of carbon with a half-life of 5700 ± 30 years (Kutschera, 2019), is a  
53 valuable tracer to distinguish fossil from modern carbon sources. Naturally produced in the upper atmosphere  
54 through the interaction of thermal neutrons with nitrogen, <sup>14</sup>C is finally oxidized to <sup>14</sup>CO<sub>2</sub>, which can be integrated  
55 into the biosphere via photosynthesis and into the hydrosphere via gas exchange at the water-atmosphere interface  
56 (Graven et al., 2020). On the one hand, fossil fuels (e.g. coal, oil, natural gas) that were formed millions of years  
57 ago are now devoid of <sup>14</sup>C because of its short half-life compared to geological time scales. On the other hand,  
58 CO<sub>2</sub> and CH<sub>4</sub> derived from fresh organic matter contain <sup>14</sup>C/<sup>12</sup>C ratios close to the current atmospheric <sup>14</sup>CO<sub>2</sub>  
59 signature. Atmospheric <sup>14</sup>CO<sub>2</sub> and <sup>14</sup>CH<sub>4</sub> measurements are thus valuable proxies to study the different sources of  
60 CO<sub>2</sub> and CH<sub>4</sub> released to the atmosphere.

61 Atmospheric <sup>14</sup>CO<sub>2</sub> measurements have a long history. Since the first measurements focused on the documentation  
62 of the atmospheric <sup>14</sup>CO<sub>2</sub> bomb peak in the 1950s-1960s associated with nuclear bomb tests (Levin et al., 1985;  
63 Manning et al., 1990; Nydal and Lövseth, 1983), there are now international monitoring programs following the  
64 long-term evolution of atmospheric <sup>14</sup>CO<sub>2</sub> at background sites (e.g., Hammer et al., 2017; Turnbull et al., 2007).  
65 Observations at the High-Altitude Research Station Jungfraujoch (JFJ) in Switzerland have been conducted since  
66 1986; there, two-weeks integrated CO<sub>2</sub> samples have been collected and further purified and analyzed at the  
67 Heidelberg laboratory (Germany) (Levin et al., 2013, 2023). On a more local scale, atmospheric <sup>14</sup>CO<sub>2</sub>  
68 measurements have been used to study CO<sub>2</sub> emissions from urban areas to entire countries (Basu et al., 2020;  
69 Graven et al., 2018; Levin et al., 2003). Since the bomb peak in the middle of the last century, Δ<sup>14</sup>CO<sub>2</sub> values have  
70 been declining mostly due to the emissions of <sup>14</sup>C-free fossil fuel CO<sub>2</sub>, which depletes the atmospheric Δ<sup>14</sup>CO<sub>2</sub>  
71 signal (Levin et al., 2010).

72 Atmospheric measurements of <sup>14</sup>CH<sub>4</sub> have been more limited than <sup>14</sup>CO<sub>2</sub> so far. One reason for this is related to  
73 the about 200-times lower atmospheric CH<sub>4</sub> concentration compared to CO<sub>2</sub>: while 2-5 liters of air are sufficient  
74 to analyze <sup>14</sup>CO<sub>2</sub> (e.g. yielding about 1 mgC from 5 L air at 420 ppm CO<sub>2</sub>), several tens of liters are required for  
75 <sup>14</sup>CH<sub>4</sub> analysis (e.g. yielding about 50 µgC from 50 L air at 2 ppm CH<sub>4</sub>). The sampling and analysis of <sup>14</sup>CH<sub>4</sub> is  
76 therefore difficult, and prone to CO<sub>2</sub> contamination. Besides this technical consideration, the interpretation of  
77 atmospheric <sup>14</sup>CH<sub>4</sub> measurements may be complicated at study sites that are influenced by nuclear power plants  
78 (NPPs) (Eisma et al., 1994, 1995; Levin et al., 1992). Pressurized water reactors (PWRs), which are currently the  
79 most widely operated plants (IAEA PRIS, 2025), emit <sup>14</sup>C mainly as <sup>14</sup>CH<sub>4</sub>, whereas other reactor types emit <sup>14</sup>C  
80 mainly as <sup>14</sup>CO<sub>2</sub> (Vance et al., 1995; Zazzeri et al., 2018). The annual global nuclear <sup>14</sup>C emission rate for 2016  
81 has been estimated to about 105 TBq for <sup>14</sup>CO<sub>2</sub> and about 45 TBq for <sup>14</sup>CH<sub>4</sub> (Zazzeri et al., 2018). Although <sup>14</sup>CO<sub>2</sub>  
82 emissions are larger, the influence of nuclear <sup>14</sup>CH<sub>4</sub> emissions on atmospheric <sup>14</sup>CH<sub>4</sub> is stronger due to the much  
83 lower atmospheric CH<sub>4</sub> concentration compared to CO<sub>2</sub>. This also explains why current atmospheric <sup>14</sup>C/<sup>12</sup>C ratios  
84 are about 35% higher for <sup>14</sup>CH<sub>4</sub> than <sup>14</sup>CO<sub>2</sub> (Emmenegger et al., 2025a; Gonzalez Moguel et al., 2022).

85 Despite these challenges, several analysis setups and atmospheric <sup>14</sup>CH<sub>4</sub> datasets have been reported from ice cores  
86 and atmospheric samples. In the 1990s, Levin et al. (1992) reported, in particular, first sporadic <sup>14</sup>CH<sub>4</sub>  
87 measurements between 1988 and 1991 at JFJ. Eisma et al. (1994, 1995) measured atmospheric <sup>14</sup>CH<sub>4</sub> values from  
88 a tall tower in the Netherlands and highlighted the challenge to interpret <sup>14</sup>CH<sub>4</sub> measurements, even when using  
89 an atmospheric transport model to evaluate the nuclear influence on the measurements. Lassey et al. (2007a, b)  
90 compiled more than 200 individual atmospheric <sup>14</sup>CH<sub>4</sub> measurements from the Northern and Southern  
91 Hemispheres between 1986 and 2000 and deduced that about 30% of the global CH<sub>4</sub> source for this period had a  
92 fossil origin. Hmiel et al. (2020) used <sup>14</sup>CH<sub>4</sub> measurements from ice cores to better constrain natural geological  
93 (i.e., fossil) CH<sub>4</sub> emissions during the preindustrial era. By synthesizing atmospheric CH<sub>4</sub> concentration and its  
94 major isotopologues (<sup>13</sup>CH<sub>4</sub>, CH<sub>3</sub>D and <sup>14</sup>CH<sub>4</sub>) for 1750-2015, Fujita et al. (2025) estimated 30 % lower global  
95 CH<sub>4</sub> emissions from the fossil-fuel industry compared to previous isotope-based studies. Another output of their



96 work was an updated inventory of the nuclear  $^{14}\text{CH}_4$  emissions between 1960 and 2015 based on nuclear electricity  
97 production data.

98 In recent years, several novel analysis systems and studies for  $^{14}\text{CH}_4$  have been reported (Espic et al., 2019;  
99 Gonzalez Moguel et al., 2022; Zazzeri et al., 2021, 2023) increasing the analysis capabilities, even in a more field-  
100 compatible way (Zazzeri et al., 2025). Despite these new studies, recent background atmospheric  $^{14}\text{CH}_4$  values are  
101 still missing. At the Laboratory for the Analysis of Radiocarbon with AMS (LARA, University of Bern) (Szidat,  
102 2020), a system exists since 2019 to analyze  $^{14}\text{CH}_4$  and  $^{14}\text{CO}_2$  from a single atmospheric sample (Espic et al., 2019)  
103 and was already used in several studies (Espic et al., 2025; Etiope et al., 2024; Zazzeri et al., 2025). Here, we  
104 present atmospheric  $^{14}\text{CH}_4$  and  $^{14}\text{CO}_2$  measurements conducted at the High-Altitude Research Station Jungfraujoch  
105 between 2019 and 2024, discuss their representativeness regarding the nuclear influence in Europe and show their  
106 relevance as worldwide background values.

107

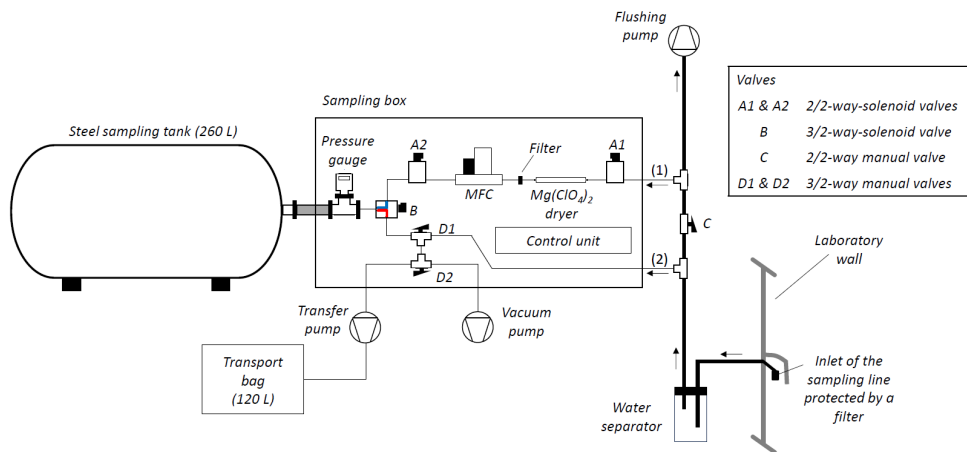
108 **2. Material & Methods**

109 **2.1. Jungfraujoch Site and Sampling Strategy**

110 The High-Altitude Research Station Jungfraujoch (stretching from 3455 to 3585 m a.s.l.,  $46^{\circ}32'51''\text{N}$ ,  $7^{\circ}59'7''\text{E}$ ,  
111 JFJ), established in 1931, is located on a mountain ridge in the Swiss Alps. Among others, this station is part of  
112 the Global Atmosphere Watch (GAW) network as well as of the Network for the Detection of Atmospheric  
113 Composition Change (NDACC). Furthermore, JFJ is labelled as an Class 1 Station of the European-wide Integrated  
114 Carbon Observation System (ICOS) Research Infrastructure (Heiskanen et al., 2022) since May 2018 (Yver-Kwok  
115 et al., 2021). Because of its high elevation, JFJ is a well-recognized international background station (Leuenberger  
116 and Flückiger, 2008). However, it is also intermittently impacted by direct transport from the polluted planetary  
117 boundary layer, most frequently during daytime from April to September (Henne et al., 2010).

118 A biweekly air sampling program measuring  $^{14}\text{CH}_4$  and  $^{14}\text{CO}_2$  at JFJ every two weeks started in January 2019.  
119 Until March 2023, two morning grab air samples were taken using a membrane pump (N022AN.18, KNF  
120 Neuberger AG, Germany) that directly pumped air from the Sphinx terrasse (3580 m a.s.l.) at JFJ into two PE-Al-  
121 PE 120 L bags (Tecobag, Tesseraux Spezialverpackungen GmbH, Germany) through a dedicated sampling line  
122 (Synflex Decabon 1300 Tubing, OD = 6 mm). The sampled air was dried with a magnesium perchlorate dryer  
123 ( $\text{Mg}(\text{ClO}_4)_2$ , ACS reagent, ThermoFisher, USA) to avoid condensation and further reactions between water vapor  
124 and other sampled gas species. The sampling duration per bag was commonly between 20 and 55 min depending  
125 on the ambient pressure, temperature and the flow resistance during sampling due to the dryer and the long length  
126 and small diameter of the sampling line. The morning grab samplings were performed manually and as early as  
127 possible in the morning to avoid the influence of the daytime planetary boundary layer; in practice, it commonly  
128 occurred between 7:00 and 10:00 UTC, depending on the seasonal train schedule ensuring the public transport up  
129 to JFJ.

130 To increase the reproducibility of the air sampling procedure and its representativeness as a background  
131 measurement, an automated air sampling system was developed replacing the manual sampling from April 18<sup>th</sup>  
132 onwards (Fig. 1). Its development was guided by two principles: (1) air sampling should occur passively,  
133 *i.e.*, without any mechanical pumps in contact with the sampled air, thereby minimizing the risk of contamination  
134 from membrane outgassing; and (2) sampling should be restricted to nighttime when the station mostly resides  
135 within the free troposphere, allowing for the collection of temporally integrated samples over multiple days. The  
136 novel *Jungfraujoch Air Sampling System (JASS)* consisted of a custom-made electropolished steel sampling tank  
137 (260 L, L = 140 cm, OD = 51 cm, Bechtiger Edelstahl AG, Switzerland) coupled to a sampling box containing a  
138 series of valves, all controlled by a home-made control unit including a Raspberry Pi 4B module (Raspberry Pi  
139 Ltd, United Kingdom) (Fig. 1). The whole system was installed under the roof of the research station at JFJ, at  
140 about 3462 m a.s.l. (Fig. S1). Its design allows a routine integrated nighttime air sampling procedure lasting 6  
141 hours every night (between 00:00 and 06:00 UTC) over 14 days, so integrating 84 hours in total. Compared to the  
142 initial biweekly morning grab sampling strategy, integrated sampling gives a more representative air mixture for  
143 every two-week period of interest.



144

145 **Figure 1: Jungfraujoch air sampling system (JASS) used for integrated nighttime air sampling over 14 days since April**  
146 **18<sup>th</sup> 2023.**

147 The inlet of the sampling line (Synflex Decabon 1300 Tubing, OD = 12 mm, L~10 m) was protected by a dust  
148 filter (Fig. 1). A flushing membrane pump (N022AN.18, KNF Neuberger AG, Germany) continuously conveyed  
149 outside air through this sampling line and a water separator to the sampling box. Through two T-pieces (SS-12M0-  
150 3, Swagelok, USA) integrated in this sampling line, part of the sampled air could be further directed into the  
151 sampling box, either automatically using line (1), or manually using line (2) (Fig. 1). At the beginning of a  
152 sampling period, the tank was evacuated using a vacuum pump (MV 2 NT, Vacuubrand GmbH + Co KG,  
153 Germany); the end pressure was  $\leq 0.7$  mbar. During automatic air sampling, the sampling line (1) was open and  
154 worked as follows: both 2/2-way solenoid valves A1 and A2 (0330-A-02, Bürkert, Germany) were open and the  
155 3/2-way solenoid valve B (0330-F-02, Bürkert, Germany) was in the position connecting this line with the tank  
156 (blue connection, Fig. 1); the mass-flow controller (MFC, F-201DV, Bronkhorst, The Netherlands) between A1  
157 and A2 ensured a controlled air flow into the system and the increasing pressure in the tank was monitored by a  
158 pressure gauge (RPT 200 AR, Pfeiffer Vacuum, Germany); in front of the MFC, a  $Mg(ClO_4)_2$  dryer dried the  
159 sampled air and a 0.5  $\mu$ m filter (SS-4FWS-05, Swagelok, USA) protected the MFC from particulate matter. After  
160 6 hours of sampling, both A1 and A2 valves were closed. This sampling procedure was repeated every night. After  
161 14 nighttime samplings, the pressure in the tank reached 600–650 mbar. The mean ambient atmospheric pressure  
162 at JFJ was 656 mbar over the period 2019–2024 (Emmenegger et al., 2025d); we configured our passive sampling  
163 system in a way where the tank pressure was always lower than ambient pressure, otherwise the passive sampling  
164 based on the pressure difference between the tank and the ambient pressure would not work. On-site, the transfer  
165 of the sampled air from the tank into a new bag was prepared in this manner: a dedicated transfer pump (N922SPE,  
166 KNF Neuberger AG, Germany) was turned on and the manual 3/2-way valve D2 was turned to the left (Fig. 1);  
167 the position of the 3/2-way valve D1 stayed by default turned to the left. The Python script running on the  
168 Raspberry Pi was then restarted to turn on the vacuum pump and switch the 3/2-way solenoid valve B in the  
169 position connecting the tank with the pump line (red connection, Fig. 1). At this stage, the transfer pump was  
170 evacuating the tank and after ~30 s of line flushing, a bag was connected to the line for the transfer of the sampled  
171 air. After about one hour, enough air was transferred to the bag for further  $^{14}C$  analyses. It was then closed and  
172 disconnected from the transfer pump (tank pressure at around 70–90 mbar). To accelerate the evacuation of the  
173 tank and condition it again for the next sampling, the valve D2 was then turned to the right, and the vacuum pump  
174 was evacuating the tank. The system was left like this for the rest of the day and, at 23:59 UTC, valve B switched  
175 automatically back to its sampling position (blue connection, Fig. 1) (final tank pressure  $\leq 0.7$  mbar), the vacuum  
176 pump turned off and the whole system was ready to start the next sampling period. The whole sampling system  
177 was validated to be leak-tight in our laboratory in Bern before being transferred to JFJ. The low pressure achieved  
178 in the tank before each new sampling every two weeks regularly validated the tightness of the sampling system.  
179

180 **2.2. Sample preparation and measurements of  $\Delta^{14}CH_4$  and  $\Delta^{14}CO_2$**

181 For both morning grab and integrated nighttime sampling strategies, the air collected in bags was transferred to  
182 the LARA laboratory at the University of Bern (Szidat, 2020), where a dedicated extraction line for  $^{14}CH_4$  and  
183  $^{14}CO_2$  analysis was available (see Espic et al., 2019 for details). The typical air volume for one analysis was 60 L.



184 During a preconcentration step, this air was pumped successively through three traps filled either with fiber glass  
185 or activated charcoal and cooled down with liquid nitrogen; this allowed us to preserve the whole amount of CH<sub>4</sub>  
186 contained in the initial 60 L of air by trapping or pumping away the main other gas species, especially nitrogen  
187 and oxygen. CO<sub>2</sub> was quantitatively trapped in the first trap and could be collected separately (see below). After  
188 that, the gas sample volume was about 10 mL, small enough to be run through a gas chromatograph (GC, 7890B,  
189 Agilent, USA; ShinCarbon ST 80/100 packed column; thermal conductivity detector, He as carrier gas) to purify  
190 the sample. CH<sub>4</sub> was isolated quantitatively from the remaining CO and CO<sub>2</sub> present in trace quantities due to  
191 different elution times in the GC (CO: ~2 min; CH<sub>4</sub>: ~8 min; CO<sub>2</sub>: ~13 min). Downstream of the GC, the extracted  
192 pure CH<sub>4</sub> was converted into CO<sub>2</sub> by combustion in a flow oven at 950°C using copper oxide wires as a catalyst.  
193 The CH<sub>4</sub>-derived CO<sub>2</sub> (~60 to 70 µg of carbon, µgC) was transferred into glass ampoules (OD = 4 mm) and sealed  
194 for gas radiocarbon measurements. After the CH<sub>4</sub> extraction procedure, the CO<sub>2</sub> of the sample held in the first trap  
195 was recovered by cryogenic transfer into a ~55 mL glass flask. The carbon mass of the recovered CO<sub>2</sub> was typically  
196 greater than 1 mgC, which was transformed into graphite using an automated graphitization equipment (AGE)  
197 (Némec et al., 2010).

198 Radiocarbon analyses of the gaseous CH<sub>4</sub>-derived CO<sub>2</sub> samples and the graphite CO<sub>2</sub> samples were performed  
199 either at LARA or at the Laboratory of Ion Beam Physics, ETH Zürich, Switzerland, using the same type of AMS  
200 (MIni CARbon DAting System, MICADAS), equipped with a gas ion source (Ruff et al., 2007; Synal et al., 2007).  
201 Glass ampoules were cracked in a dedicated gas inlet system (Wacker et al., 2013) and the CH<sub>4</sub>-derived CO<sub>2</sub> was  
202 diluted with He to ~5%, transferred into a syringe, and then fed into the ion source using a constant gas flow.  
203 Graphite samples were introduced directly to the MICADAS source. For both types of samples, raw <sup>14</sup>C/<sup>12</sup>C as  
204 well as <sup>13</sup>C/<sup>12</sup>C ratios were converted into F<sup>14</sup>C and δ<sup>13</sup>C values, respectively, by performing a blank subtraction  
205 as well as a standard normalization and correction for isotope fractionation (only for F<sup>14</sup>C) using <sup>14</sup>C-free CO<sub>2</sub>  
206 (F<sup>14</sup>C = 0) and CO<sub>2</sub> produced from the primary NIST standard oxalic acid II (SRM 4990C) (F<sup>14</sup>C = 1.34066,  
207 δ<sup>13</sup>C = -17.8 ‰), respectively. For the gas measurements, standards came from two gas bottles directly attached  
208 to the gas inlet system; both mixtures consisted of 5% CO<sub>2</sub> with the F<sup>14</sup>C value of interest and 95% He. For the  
209 graphite measurements, both standards underwent the same sample preparation as the CO<sub>2</sub> samples and were  
210 measured with them in the same magazine. The final data evaluation was done using the BATS tool (Wacker et  
211 al., 2010). The typical measurement precision is 8 ‰ for <sup>14</sup>CH<sub>4</sub> and 1.5 ‰ for <sup>14</sup>CO<sub>2</sub> (see below). Throughout the  
212 current work, <sup>14</sup>C results are reported using the notation Δ<sup>14</sup>C, and calculated with age correction as the parameter  
213 Δ in Stuiver and Polach (1977) and in equation 29 in Stenström et al. (2011).  
214

### 215 2.3. Ancillary measurements and datasets

216 At JFJ, in the framework of the ICOS measurement program, CO<sub>2</sub> and CH<sub>4</sub> concentrations are measured  
217 continuously using cavity ringdown spectroscopy; corresponding hourly average values were used in the present  
218 study (Emmenegger et al., 2025b, c). Furthermore, integrated samples have been collected since 1986 to analyze  
219 atmospheric Δ<sup>14</sup>CO<sub>2</sub>, first started by the University of Heidelberg, now run as part of the ICOS Research  
220 Infrastructure (Emmenegger et al., 2025a; Hammer et al., 2017; Levin and Kromer, 2004). The dedicated setup  
221 draws ambient air throughout 14 days through a sodium hydroxide solution, in which CO<sub>2</sub> is chemically absorbed.  
222 We chose the same 14-day schedule for our nighttime sampling as the ICOS schedule to enable a comparison  
223 between both datasets. ICOS Δ<sup>14</sup>CO<sub>2</sub> values are also reported as Δ values according to Stuiver and Polach (1977).

224 We also made use of continuous <sup>222</sup>Radon (in the following referred as Rn) measurements at JFJ with a two-filter  
225 dual loop alpha particle detector, operated by the University of Basel since 2009 (Griffiths et al., 2014) and which  
226 is meanwhile part of ICOS (Fig. S1). Rn is emitted from land surfaces into the atmosphere and because of its half-  
227 life of 3.8 days, it is a potential tracer of recent land contact. In this study, Rn was used as a proxy to distinguish  
228 atmospheric conditions mostly influenced by free tropospheric conditions from conditions mostly influenced by  
229 the planetary boundary layer (*i.e.*, with recent land contact). To account for variations in ambient temperature and  
230 pressure, the raw hourly Rn concentrations (Conen, 2025) were converted into Rn values at STP conditions (*i.e.*,  
231 T = 0°C, P = 101'325 Pa).

232 To evaluate the accuracy and stability of our Δ<sup>14</sup>CH<sub>4</sub> and Δ<sup>14</sup>CO<sub>2</sub> measurements over time, regular measurements  
233 of a pressurized air bottle (PAB) (Carbagas, Switzerland) considered as an internal standard have been performed  
234 since March 2022 in parallel to the measurements of the JFJ samples; this air strictly underwent the same extraction  
235 and measurement procedures as the JFJ samples. A first bottle was measured until end of July 2023  
236 (CH<sub>4</sub> = 1997 ± 2 ppb, and CO<sub>2</sub> = 434.5 ± 0.1 ppm), replaced by a second one in August 2023 (CH<sub>4</sub> = 2178 ± 2 ppb,



237 and  $\text{CO}_2 = 455.8 \pm 0.1 \text{ ppm}$ ). It should be noted that the  $\Delta^{14}\text{CH}_4$  and  $\Delta^{14}\text{CO}_2$  values of both bottles were *a priori*  
238 unknown and that we used them to evaluate the stability of the values derived from our measurement procedure.

239 **2.4. Atmospheric modeling of nuclear  $^{14}\text{C}$  influence at JFJ**

240 One goal of the present study was to evaluate the influence of nuclear  $^{14}\text{CH}_4$  and  $^{14}\text{CO}_2$  emissions on our  
241 atmospheric  $\Delta^{14}\text{CH}_4$  and  $\Delta^{14}\text{CO}_2$  measurements at JFJ. For this purpose, the amount and transport of  $^{14}\text{CH}_4$  and  
242  $^{14}\text{CO}_2$  molecules from nuclear emissions were simulated using the Lagrangian particle dispersion model FLEXible  
243 PARTicle (FLEXPART) (Pisso et al., 2019) in the version adopted for inputs from the numerical weather prediction  
244 model COSMO (Henne et al., 2016). Here, we use the COSMO analysis product of the Swiss Federal Office of  
245 Meteorology and Climatology (MeteoSwiss), based on high spatial resolution (1 km x 1 km) model simulations  
246 and using a local ensemble transform Kalman filter (LETKF) meteorological data assimilation system (Schraff et  
247 al., 2016). Meteorological analysis fields from this product were available at 1 hour temporal resolution for the  
248 Alpine domain (approximately 0-17°E, 42-50°N). The FLEXPART-COSMO model was used in previous  
249 atmospheric studies including the verification of the Swiss  $\text{CH}_4$  emission inventory (Henne et al., 2016), the  
250 influence of nuclear  $^{14}\text{CO}_2$  emissions on  $\Delta^{14}\text{CO}_2$  at a Swiss tall tower (Berhanu et al., 2017), the analysis of  $\text{CO}_2$   
251 and  $\delta^{13}\text{CO}_2$  at JFJ (Pieber et al., 2022), and for inverse modeling of halocarbon emissions over Switzerland  
252 (Katharopoulos et al., 2023). Here, the model was operated in the same way as in Katharopoulos et al. (2023). In  
253 short, 50'000 model particles were released continuously from JFJ for every 3-hour interval and traced backwards  
254 in time for 4 days or until they reached the domain boundaries. Afterwards, the integration of the particles' path  
255 was continued for up to 10 days in a European scale FLEXPART-IFS simulation driven by hourly inputs from the  
256 European Centre for Medium-Range Weather Forecasts (ECMWF) HRES operational forecast/analysis product  
257 available at 0.1°x0.1° resolution. The residence time of particles below a height of 50 m above model ground is  
258 then estimated in 3-hourly intervals and divided by air density provides so called source sensitivities (or  
259 concentration footprints).

260 Nuclear  $^{14}\text{C}$  emissions between 2019 and 2023 from the nuclear power plants (NPPs) located in the modeling area  
261 (Fig. S2) were mostly estimated using the compilation of nuclear  $^{14}\text{C}$  emissions of Laemmel et al. (2025). The  
262 atmospheric transport modeling was performed only for the period 2019-2023, as the input parameters for 2024  
263 were not yet fully available. For most countries (Bulgaria, the Czech Republic, Romania, Slovakia, Slovenia,  
264 Spain, the Netherlands, and the United Kingdom) only annual total  $^{14}\text{C}$  emissions for the NPPs were available. For  
265 some countries, more detailed information could be used including quarterly  $^{14}\text{C}$  emissions from NPPs in France  
266 and Germany and monthly emissions for the Swiss NPPs Leibstadt and Gösgen, the Swedish NPPs Forsmark,  
267 Oskarshamn, and Ringhals, some NPPs in the United Kingdom and the French nuclear fuel reprocessing plant  
268 (NFRP) La Hague. Monthly inorganic and organic  $^{14}\text{C}$  emissions from the Hungarian NPP Pak were also available  
269 for 2019 in this dataset. In addition to these published values, monthly inorganic and organic  $^{14}\text{C}$  emissions for  
270 2020-2023 were kindly made available by the operating company of the NPP Pak for this simulation. Reported  
271 emissions from the NPPs located in Belarus, Belgium, Russia, and Ukraine were not available; we estimated the  
272 annual  $^{14}\text{C}$  emissions for each of these plants by multiplying the annual electricity production (Laemmel and  
273 Szidat, 2025) by reactor-specific emission factors (EF) of 0.19, 0.41, and 1.3 TBq/GWa (GWa = gigawatt x 1 year)  
274 for PWR, VVER (water-cooled water-moderated energy reactor), and LWGR (light water graphite reactor),  
275 respectively. EF values for PWR and VVER were derived from the work of Fujita et al. (2025) and EF value for  
276 LWGR from the work of Zazzeri et al. (2018).

277 In a further step,  $^{14}\text{CH}_4$  and  $^{14}\text{CO}_2$  emissions per NPP were derived, as the reported values were mainly for total  
278  $^{14}\text{C}$ . We used data for inorganic and organic  $^{14}\text{C}$  emissions that were reported in some countries (e.g. for NPPs in  
279 Germany, Hungary, Spain, Sweden, and Switzerland). For other countries we assumed that PWRs and VVERs emit  
280 75 % of the total  $^{14}\text{C}$  amount in organic form (so 25 % in inorganic form) and that all the other reactors (e.g. boiling  
281 water reactor (BWR), LWGR, and pressurized heavy water reactor (PHWR)) emit  $^{14}\text{C}$  entirely in inorganic form,  
282 as also was assumed by Fujita et al. (2025). Furthermore, we assumed that the inorganic  $^{14}\text{C}$  form is entirely  
283 composed of  $^{14}\text{CO}_2$  and that  $^{14}\text{CH}_4$  represents 72.5 % of the organic  $^{14}\text{C}$  form; this last value was derived from the  
284 study of Kunz (1985) who analysed the composition of hydrocarbons of gaseous effluents at two PWRs in the  
285 USA. They reported values of 68 and 77 % at the PWR Ginna and PWR Indian Point, respectively. Finally, the  
286 annual, quarterly or monthly emission amount of  $^{14}\text{CO}_2$  and  $^{14}\text{CH}_4$  available for each plant was equally divided  
287 into three-hour intervals to compute an emission rate per output step of the FLEXPART transport simulation.  
288 FLEXPART-derived source sensitivities, convoluted with these emission rates yield  $^{14}\text{C}$  mole fractions at the  
289 sampling site and a nuclear correction for  $\Delta^{14}\text{C}^{\text{Nuc}}$  can be calculated assuming a mass balance model for C and  $^{14}\text{C}$   
290 (Graven et al., 2019):



291 
$$\Delta^{14}C^{Nuc} = \frac{\Delta_n^{14}C_n}{c_{obs}}$$
 (1)

292 where  $\Delta_n$  is the  $\Delta^{14}C$  signature that a pure  $^{14}\text{C}$  sample would have. For a pure  $^{14}\text{CO}_2$  sample, following Levin et  
293 al. (2010), we used an estimate of  $\Delta_n$  of  $8.21 \times 10^{14} \text{‰}$ , assuming a constant  $\delta^{13}\text{C}$  value of  $-8\text{‰}$ . For a pure  $^{14}\text{CH}_4$   
294 sample, based on a similar calculation, we used an estimate of  $\Delta_n$  of  $8.89 \times 10^{14} \text{‰}$ , assuming a constant  $\delta^{13}\text{C}$   
295 value of  $-48\text{‰}$ .

296 **2.5. Background atmospheric  $\Delta^{14}\text{CH}_4$  modeling**

297 Another goal of the present study was to evaluate the representativeness of our atmospheric  $\Delta^{14}\text{CH}_4$  measurements  
298 at JFJ on a global level. For this goal, we compared our data with calculated atmospheric  $\Delta^{14}\text{CH}_4$  values from a  
299 one-box model developed by Fujita et al. (2025). In this study, we extended their simulation until 2024 (Fig. S3)  
300 by updating their posterior  $\text{CH}_4$  emission scenarios since 2013 (*i.e.*, average of posterior CEDS, EDGARv5, and  
301 EDGARv6 scenarios; see Fujita et al. (2025)). The anthropogenic  $\text{CH}_4$  emissions for 2013-2022 were extended by  
302 using EDGARv8 (European Commission. Joint Research Centre., 2023). To match the consistency with the  
303 posterior anthropogenic biogenic (BIO) and fossil fuel (FF) emissions in Fujita et al. (2025), the mean differences  
304 between EDGARv8 and Fujita et al. (2025) were calculated for 2008-2012 (BIO: 2.1 Tg/yr, FF: 9.8 Tg/yr) and  
305 then added to the values of EDGARv8 after 2013, respectively. For 2023-2024, the emissions of the Shared  
306 Socioeconomic Pathways (SSPs) were used. Here, we adopted SSP5-8.5 scenario in 2030 (Gidden et al., 2019)  
307 and linearly interpolated it between the EDGARv8 2022 emissions and the 2030 scenario emissions to the years  
308 2023 and 2024. Natural biogenic  $\text{CH}_4$  emissions were optimized based on the  $\text{CH}_4$  mass balance equation to keep  
309 the consistency between our simulations and observed global mean  $\text{CH}_4$  mole fractions by NOAA/GML (Lan et  
310 al., 2025a). To evaluate the  $^{14}\text{C}$  signature of the biospheric  $\text{CH}_4$  sources,  $\Delta^{14}\text{CO}_2$  values for the time period 2013-  
311 2024 were derived from the SSP5-8.5 scenario (Graven et al., 2020). To extend the nuclear  $\Delta^{14}\text{CH}_4$  emissions beyond  
312 2013, we considered the posterior annual nuclear  $\Delta^{14}\text{CH}_4$  emissions derived by Fujita et al. (2025). Assuming that  
313 only PWRs and VVERs are emitting  $^{14}\text{CH}_4$ , a mean annual emission factor  $\phi$  (GBq/GWa) was computed by  
314 dividing these emissions by the annual total electricity production by PWRs and VVERs derived from the data  
315 compilation by Laemmel and Szidat (2025). Considering the years 2008-2012, the mean  $\phi$  value was  
316 250 GBq/GWa, the min  $\phi$  value was 243 GBq/GWa, and the max  $\phi$  value was 259 GBq/GWa. Considering these  
317 three  $\phi$  values and the annual total electricity production by PWRs and VVERs in 2013-2024 (the value for 2024  
318 was chosen equal to 2023 as the real value was not yet available), three projections of annual nuclear  $\Delta^{14}\text{CH}_4$   
319 emissions were computed and used as variable input parameter in three different simulations of global atmospheric  
320  $\Delta^{14}\text{CH}_4$  values (Fig. S3g). Posterior geologic emissions, biospheric turnover time, total  $\text{CH}_4$  lifetime, carbon and  
321 hydrogen kinetic isotope effects, and carbon and hydrogen  $\text{CH}_4$  isotopic signatures for respective sources in Fujita  
322 et al. (2025) were repeated by the values in 2012 over 2013-2024.

323 The simulated  $\Delta^{14}\text{CH}_4$  values were compared to our annual mean  $\Delta^{14}\text{CH}_4$  values at JFJ for 2019-2024 and  
324 previously reported measurements from ice cores of Greenland and Antarctica (Hmiel et al., 2020) and from  
325 atmospheric samples (Gonzalez Moguel et al., 2022; Lassey et al., 2007b; Levin et al., 1992; Quay et al., 1999;  
326 Sparrow et al., 2018; Townsend-Small et al., 2012; Wahnen et al., 1989). Note that the data in Hmiel et al. (2020)  
327 was used in Fujita et al. (2025) as observational constraints. Several other studies were found but not used here  
328 because of the large scatter in the reported data (Lowe et al., 1988; Manning et al., 1990) or difficulties in the unit  
329 conversion into current radiocarbon parameters (Ehhalt, 1974).

330

331 **3. Results**

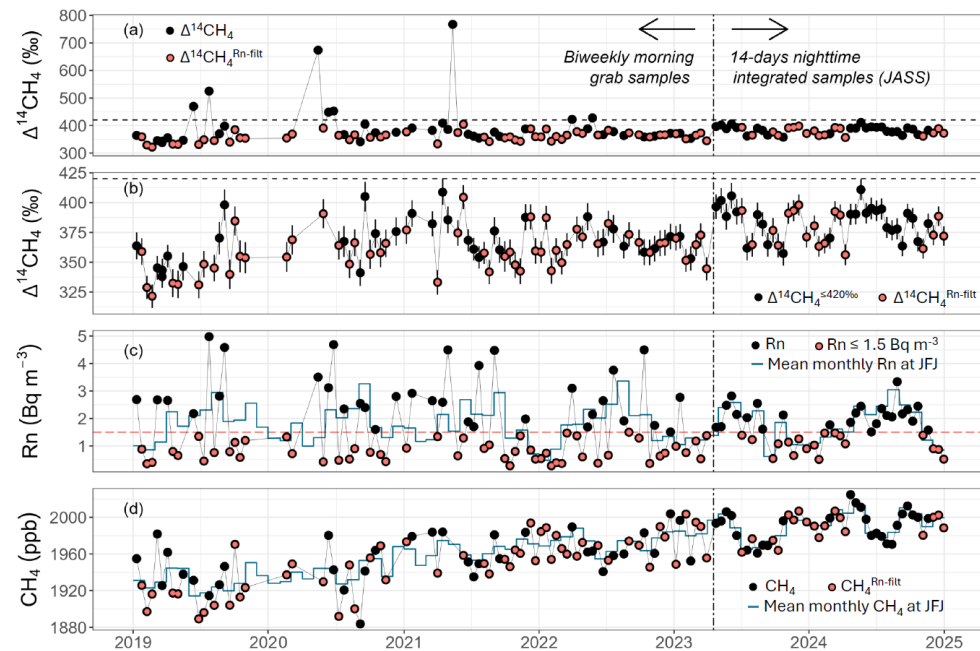
332 **3.1.  $\Delta^{14}\text{CH}_4$  measurements at Jungfraujoch**

333  $\Delta^{14}\text{CH}_4$  values at JFJ between 2019 and 2024 were between 322 and 767  $\text{‰}$  and showed a slightly increasing trend  
334 over the last six years (Fig. 2a,b). Some exceptionally high  $\Delta^{14}\text{CH}_4$  values were measured (*i.e.*, on June 13<sup>th</sup> and  
335 July 25<sup>th</sup> 2019; May 13<sup>th</sup>, June 10<sup>th</sup> and June 24<sup>th</sup> 2020; May 12<sup>th</sup> 2021) and were attributed to local and strong  
336 nuclear  $\Delta^{14}\text{CH}_4$  releases. Rn values were lower than  $5 \text{ Bq m}^{-3}$  over 2019-2024 with generally lower values during  
337 winter months compared to summer months (Fig. 2c), which is consistent with a potentially stronger influence of  
338 the planetary boundary layer in summer. Annual mean  $\text{CH}_4$  concentrations increased from 1930 ppb in 2019 to



339 1996 ppb in 2024 (Fig. 2d). Rn and CH<sub>4</sub> concentration data shown here represent the corresponding average values  
 340 during the sampling intervals.

341 Reduced scatter in Δ<sup>14</sup>CH<sub>4</sub> values since the installation of the JASS in April 2023 is visible (Fig. 2a,b). Also, hourly  
 342 Rn and CH<sub>4</sub> concentrations averaged over the JASS sampling periods show less amplitude variation after this date.  
 343 For both parameters, corresponding values are closer to the monthly means measured *in situ* by the ICOS  
 344 instruments (blue curves in Fig. 2c,d). The temporal stability of our Δ<sup>14</sup>CH<sub>4</sub> measurements from March 2022  
 345 onwards is evaluated using the regular Δ<sup>14</sup>CH<sub>4</sub> measurements of our two internal standard PAB bottles. The  
 346 standard deviation of the Δ<sup>14</sup>CH<sub>4</sub> value for all 40 CH<sub>4</sub> measurements over 15 months for each PAB bottle (so about  
 347 80 CH<sub>4</sub> measurements in total) is 8 ‰ (Fig. S4a,b), which is lower than the instrumental uncertainty of a single  
 348 Δ<sup>14</sup>CH<sub>4</sub> measurement (12 ‰) indicating the satisfactory temporal reliability of our Δ<sup>14</sup>CH<sub>4</sub> measurements.



349  
 350 Figure 2: (a) All Δ<sup>14</sup>CH<sub>4</sub> values (black points) measured at JFJ since 2019; (b) same Δ<sup>14</sup>CH<sub>4</sub> values excluding the points  
 351 showing a clear nuclear influence (black points, Δ<sup>14</sup>CH<sub>4</sub>≤420‰). (c) Rn and (d) CH<sub>4</sub> concentrations corresponding to the  
 352 sampling periods of the Δ<sup>14</sup>CH<sub>4</sub> measurements. The vertical black dashed line in all the four subplots on April 18<sup>th</sup>, 2023  
 353 represents the beginning of air sampling using the new JASS system. The horizontal dashed line in (a) and (b) is shown  
 354 for Δ<sup>14</sup>CH<sub>4</sub> = 420 ‰, i.e., the chosen threshold for a clear influence of nuclear contamination. The horizontal red dotted  
 355 line in (c) is shown at 1.5 Bq m<sup>-3</sup> Rn, the chosen threshold between free-troposphere conditions and conditions  
 356 influenced by the planetary boundary layer at JFJ. Red points in all the subplots represent Δ<sup>14</sup>CH<sub>4</sub>, Rn, and CH<sub>4</sub> values  
 357 where corresponding Rn values are lower than 1.5 Bq m<sup>-3</sup>. Blue lines in (c) and (d) correspond to the monthly means  
 358 measured *in situ*.

359 For 2019-2024, mean annual atmospheric Δ<sup>14</sup>CH<sub>4</sub> values can be deduced from our biweekly air sampling program  
 360 in different ways (Table 1). Firstly, all Δ<sup>14</sup>CH<sub>4</sub> measurements clearly influenced by nuclear contamination were  
 361 excluded. Choosing a threshold of 420 ‰ (Δ<sup>14</sup>CH<sub>4</sub>≤420‰, Fig. 2b and 3) 129 of the 137 measurements initially  
 362 available are retained (94 %). Over the six years, a slightly increasing Δ<sup>14</sup>CH<sub>4</sub>≤420‰ tendency rising from  
 363 350 ± 19 ‰ in 2019 to 381 ± 13 ‰ in 2024 (*i.e.*, by a rate of ~+6 ‰/yr) is observed (Table 1, Fig. 3).

364 Secondly, only Δ<sup>14</sup>CH<sub>4</sub> measurements from Δ<sup>14</sup>CH<sub>4</sub>≤420‰ values whose corresponding Rn values are lower than  
 365 1.5 Bq m<sup>-3</sup> STP (Δ<sup>14</sup>CH<sub>4</sub><sup>Rn-filt</sup>) were retained; analyzing the probability density function of more than five years of  
 366 Rn values at JFJ (Nov 2015 to Dec 2020), Conen and Zimmermann (2020) found that air masses with  
 367 corresponding Rn values below 1.5 Bq m<sup>-3</sup> STP belong mostly to the free troposphere (with 77% confidence).  
 368 Compared to the first set of mean annual values (n = 129), mean annual Δ<sup>14</sup>CH<sub>4</sub> values are 1-7 ‰ lower and the



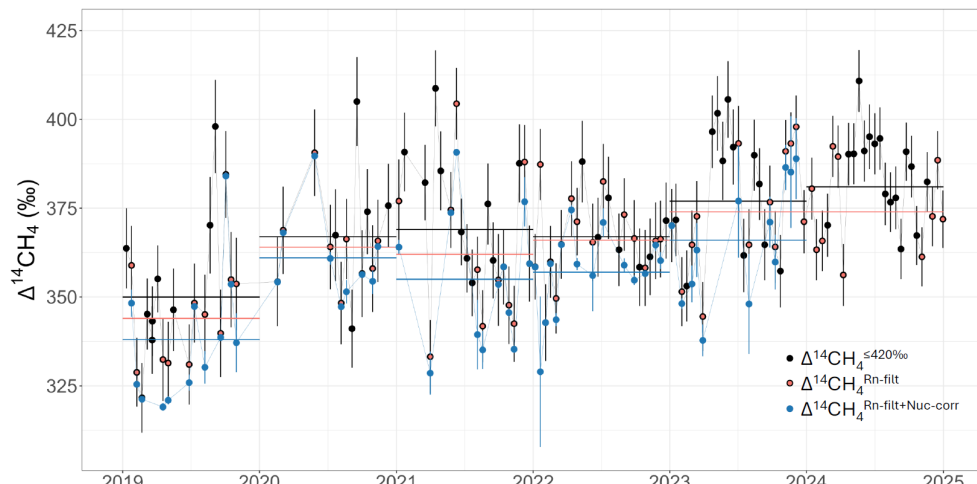
369 total number of points used for these mean values is almost halved ( $n = 71$ ) (Table 1, Fig. 3). During the period of  
 370 integrated sampling the observations removed with the Rn threshold are mainly from the summer.

371 The third processing step additionally corrects for the influence of NPPs by subtracting the nuclear  $\Delta^{14}\text{CH}_4$  signal  
 372 simulated with FLEXPART-COSMO from the  $\Delta^{14}\text{CH}_4$  measurements at JFJ. Figure 3 shows for each  $\Delta^{14}\text{CH}_4^{\text{Rn-filt}}$   
 373 value (red point) the corresponding value corrected for the nuclear influence ( $\Delta^{14}\text{CH}_4^{\text{Rn-filt} + \text{Nuc-corr}}$ ) (blue point).  
 374 Overall, the mean nuclear  $\Delta^{14}\text{CH}_4$  influence is  $7 \pm 9 \text{‰}$  (min = 0, max = 58 ‰,  $n = 60$ ).

375 **Table 1: Mean annual  $\Delta^{14}\text{CH}_4$  values with standard deviations derived from our biweekly  $\Delta^{14}\text{CH}_4$  measurements at JFJ**  
 376 **between 2019 and 2024 with three different computations. The first column of mean values only considers**  
 377  **$\Delta^{14}\text{CH}_4$  measurements  $\leq 420 \text{‰}$  ( $\Delta^{14}\text{CH}_4^{\leq 420\text{‰}}$ ). The second column additionally considers only  $\Delta^{14}\text{CH}_4$  values whose**  
 378 **corresponding Rn values are lower than  $1.5 \text{ Bq m}^{-3}$  STP ( $\Delta^{14}\text{CH}_4^{\text{Rn-filt}}$ ). The third column additionally subtracts from**  
 379 **each  $\Delta^{14}\text{CH}_4^{\text{Rn-filt}}$  value the modelled nuclear  $^{14}\text{CH}_4$  influence ( $\Delta^{14}\text{CH}_4^{\text{Rn-filt} + \text{Nuc-corr}}$ ). The numbers in brackets in columns**  
 380 **3, 4 and 5 represent the number of values per year considered for the annual mean calculation. For 2023, the last**  
 381 **sampling period finished early 2024 when no modelled nuclear  $^{14}\text{CH}_4$  influence was yet available so that the**  
 382 **corresponding  $\Delta^{14}\text{CH}_4$  value was not considered.**

Year	Number of values per year	Mean $\Delta^{14}\text{CH}_4^{\leq 420\text{‰}}$	Mean $\Delta^{14}\text{CH}_4^{\text{Rn-filt}}$	Mean $\Delta^{14}\text{CH}_4^{\text{Rn-filt} + \text{Nuc-corr}}$
		$\Delta^{14}\text{CH}_4 \leq 420 \text{‰}$	$\Delta^{14}\text{CH}_4 \leq 420 \text{‰} \& \text{Rn} \leq 1.5 \text{ Bq m}^{-3}$	$\Delta^{14}\text{CH}_4 \leq 420 \text{‰} \& \text{Rn} \leq 1.5 \text{ Bq m}^{-3} \& \text{Nuc-corrected}$
2019	22	$350 \pm 19$ (20)	$344 \pm 17$ (12)	$338 \pm 19$ (12)
2020	17	$367 \pm 16$ (14)	$364 \pm 12$ (9)	$361 \pm 13$ (9)
2021	23	$369 \pm 20$ (22)	$362 \pm 21$ (12)	$355 \pm 19$ (12)
2022	24	$367 \pm 11$ (22)	$366 \pm 12$ (15)	$357 \pm 11$ (15)
2023	25	$377 \pm 17$ (25)	$374 \pm 17$ (13)	$366 \pm 17$ (12)
2024	26	$381 \pm 13$ (26)	$374 \pm 13$ (10)	-
n	137	129	71	60

383



384

385 **Figure 3: Nuclear influence on background  $\Delta^{14}\text{CH}_4$  measurements at JFJ with values  $\leq 420 \text{‰}$  ( $\Delta^{14}\text{CH}_4^{\leq 420\text{‰}}$ ) (black**  
 386 **points). Red symbols denote points where Rn is lower than  $1.5 \text{ Bq m}^{-3}$  STP ( $\Delta^{14}\text{CH}_4^{\text{Rn-filt}}$ ) (same as in Fig. 2a,b). Black**  
 387 **error bars show  $\Delta^{14}\text{CH}_4$  measurement uncertainty. Blue points correspond to the red points after subtraction of the**  
 388 **simulated nuclear influence ( $\Delta^{14}\text{CH}_4^{\text{Rn-filt} + \text{Nuc-corr}}$ ). Blue error bars represent the standard deviation of the nuclear**  
 389 **influence. Horizontal black, red and blue lines show the annual mean values derived from the black (Table 1,**  
 390  **$\Delta^{14}\text{CH}_4^{\leq 420\text{‰}}$ ), red (Table 1,  $\Delta^{14}\text{CH}_4^{\text{Rn-filt}}$ ) and blue points (Table 1,  $\Delta^{14}\text{CH}_4^{\text{Rn-filt} + \text{Nuc-corr}}$ ), respectively.  $\Delta^{14}\text{CH}_4^{\text{Rn-filt} + \text{Nuc-corr}}$**   
 391 **values were not available for 2024 due to missing input parameters for the nuclear simulation for this year.**



392      **3.2. Comparison with previous observations and simulated global  $\Delta^{14}\text{CH}_4$  signal**

393      Our annual mean  $\Delta^{14}\text{CH}_4$  values at JFJ are similar to previous observations in the Northern Hemisphere from 2005-  
 394      2020 (Fig. 4). Direct observations from Los Angeles, Canada and Alaska showed values of 340-350 ‰,  
 395      comparable to our JFJ data of 338-366 ‰ for  $\Delta^{14}\text{CH}_4^{\text{Rn-fit} + \text{Nuc-corr}}$  from 2019-2023 (Fig. 4, Table 1). Firn air  
 396      observations from Greenland for 2005-2013 were slightly higher, 350-380 ‰, but still consistent with our data.

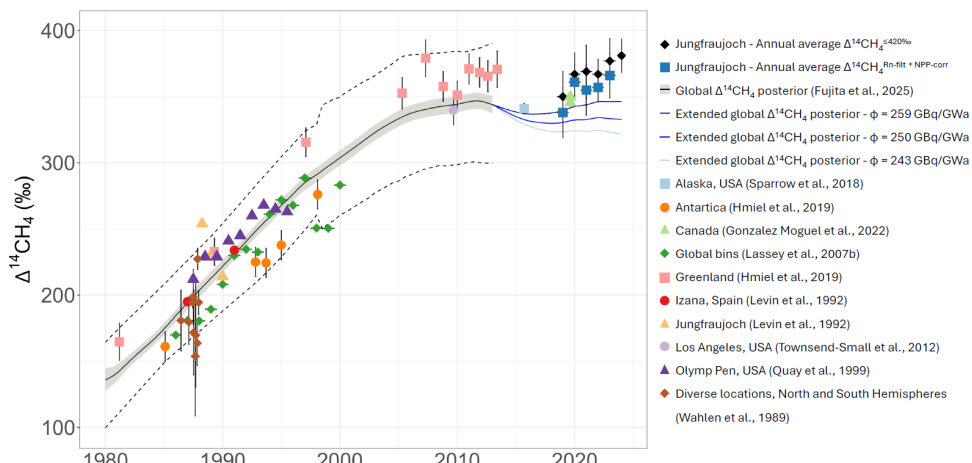
397      A rather stable global background  $\Delta^{14}\text{CH}_4$  is simulated for the period 2005-2024, supporting the consistency  
 398      between the observations over this period. This stable period followed an increase from ~140 ‰ in 1980 to ~350 ‰  
 399      in 2005 (see Fig. 4 and Fujita et al. 2025), mainly driven by increasing nuclear  $^{14}\text{CH}_4$  emissions since 1970  
 400      (Fig. S3h).

401      All the Northern Hemisphere measurement data is higher than the simulated  $\Delta^{14}\text{CH}_4$  (Fig. 4), which reflects global  
 402      atmospheric  $\Delta^{14}\text{CH}_4$  accounting for contributions from both hemispheres (Fujita et al. 2025). Due to a lack of data,  
 403      the current difference between the hemispheres is presently not well-known, but previous data indicate an excess  
 404       $\Delta^{14}\text{CH}_4$  in the Northern Hemisphere, which is consistent with stronger nuclear power plant emissions there (Fig. 4).  
 405      The observational targets from Fujita et al. (2025) were constructed to allow for this hemispheric difference and  
 406      for uncertainty due to lack of data. The mean offset between the observations in Greenland for 2005-2013 and the  
 407      simulated global  $\Delta^{14}\text{CH}_4$  value is  $22 \pm 9$  ‰, comparable to the offset between our JFJ observations for 2019-2024  
 408      and the global simulation of 0 to 33 ‰.

409      The three simulated  $\Delta^{14}\text{CH}_4$  trends from 2013 to 2024 (blue lines in Fig. 4) based on three different emission  
 410      factors  $\phi$  (Section 2.5 and Fig. S3g) show a decrease followed by a stabilization (for  $\phi = 243 \text{ GBq/GWa}$ , or a  
 411      slight increase (for  $\phi \geq 250 \text{ GBq/GWa}$ ). The initial decrease was caused by a decrease in nuclear  $^{14}\text{CH}_4$  emissions  
 412      following the Fukushima accident in 2011 (Fig. S3h). Afterwards, the stabilization or slight increase has arisen  
 413      from nuclear  $^{14}\text{CH}_4$  emissions that have increased again in particular after 2017 (Fig. S3h). Our measurement data  
 414      show a slight positive trend that is reduced after accounting for regional influences from nuclear power plant  
 415      emissions (Fig. 4, Section 3.1). The simulations seem to be more consistent with this slight positive trend from our  
 416      measurement data using the higher emission factors than the lowest emission factor, where a slight decrease in  
 417       $\Delta^{14}\text{CH}_4$  is simulated.

418      We can also compare with observations at JFJ in 1988-1991 by Levin et al. (1992) (Fig. 4). A large spread in  
 419      individual measurements of 210-255 ‰ was found at that time. We also found a large scatter in samples collected  
 420      in the morning before the installation of integrated nighttime sampling (Fig. 2, Section 3.1). The number of  
 421      operating PWRs worldwide passed from about 240 in 1991 to about 310 in 2024 (Laemmel and Szidat, 2025),  
 422      suggesting that the influence of nuclear  $^{14}\text{CH}_4$  emissions has increased. Overall, the increase from ~230 ‰ in the  
 423      1980s to 360 ‰ in the early 2020s is consistent with other data and with the simulated change (Fig. 4).

424



425



426 **Figure 4: Simulated global atmospheric  $\Delta^{14}\text{CH}_4$  signal based on the one-box model of Fujita et al. (2025) extended until**

427 2024 (see section 2.6) with observations from JFJ and other studies, for 1980-2024. The solid black line is the global

428  $\Delta^{14}\text{CH}_4$  posterior until 2013 from Fujita et al. (2025). The grey area surrounding the line shows a 68% confidence

429 interval. The dotted black lines denote the global observational target ranges, corresponding to a 99% confidence

430 interval of the global averages, defined by Fujita et al. (2025). The three blue lines represent the extrapolated global

431 atmospheric  $\Delta^{14}\text{CH}_4$  based on the three emission factor values  $\phi$  (see text). Individual points represent atmospheric

432  $\Delta^{14}\text{CH}_4$  values from atmospheric or ice-core samples. Our annual mean JFJ values between 2019 and 2024 are shown

433 as black diamonds ( $\Delta^{14}\text{CH}_4^{\leq 420\%}$ ) and blue squares ( $\Delta^{14}\text{CH}_4^{\text{Rn-filt + Nuc-corr}}$ ).

434 **3.3.  $\Delta^{14}\text{CO}_2$  measurements at Jungfraujoch**

435 Between 2019 and 2024,  $\Delta^{14}\text{CO}_2$  values measured at JFJ ranged from +3 to -17 ‰, following a decreasing trend

436 over these six years; this trend is mostly due to the emissions of  $^{14}\text{C}$ -free fossil fuel  $\text{CO}_2$  which depletes the global

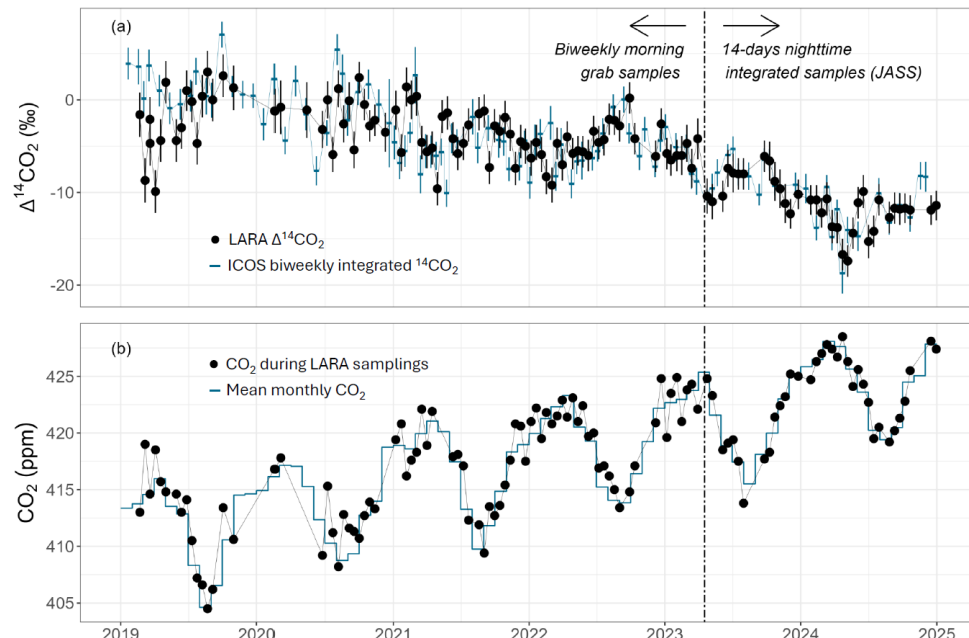
437 atmospheric  $\Delta^{14}\text{CO}_2$  signal. (Fig. 5a). Annual mean  $\text{CO}_2$  concentrations increased from 411.9 ppm in 2019 to

438 424.7 ppm in 2024 (Fig. 5b). The standard deviation of the  $\Delta^{14}\text{CO}_2$  value for all 40  $\text{CO}_2$  measurements over 15

439 months for each PAB bottle (so about 80  $\text{CO}_2$  measurements in total) is 1.5 ‰ (Fig. S4c,d), which is lower than

440 the instrumental uncertainty of a single  $\Delta^{14}\text{CO}_2$  measurement (2 ‰) indicating the satisfactory temporal reliability

441 of our  $\Delta^{14}\text{CO}_2$  measurements.



442 **Figure 5: (a) in black,  $\Delta^{14}\text{CO}_2$  values measured at JFJ since 2019 and in blue,  $\Delta^{14}\text{CO}_2$  values reported by ICOS. (b) In**

443 **black,  $\text{CO}_2$  values related to the sampling periods of our  $\Delta^{14}\text{CO}_2$  measurements and in blue, mean monthly  $\text{CO}_2$  values**

444 **measured continuously in situ. The vertical black dashed line in both subplots on April 18<sup>th</sup>, 2023 represents the change**

445 **in the sampling method, passing from biweekly morning grab air samples to 14-days nighttime integrated samples with**

446 **the JASS system.**

447 We compare our annual mean  $\Delta^{14}\text{CO}_2$  and individual  $\Delta^{14}\text{CO}_2$  observations with measurements from ICOS at JFJ

448 (Emmenegger et al., 2025a) in Figures 5a and 6 and in Table 2. The average trend in  $\Delta^{14}\text{CO}_2$  is similar in both

449 datasets:  $-2.1 \pm 1.9 \text{ ‰/yr}$  for our data and  $-2.8 \pm 1.9 \text{ ‰/yr}$  for ICOS data. Annual mean values differ by less than

450 1.5 ‰ except for 2019, when our annual mean  $\Delta^{14}\text{CO}_2$  value was 3.6 ‰ lower than the ICOS annual mean. Larger

451 individual differences are visible especially in the first half of 2019 (Fig. 5a). The offset in 2019 was probably due

452 to a small fossil contamination in our early  $\Delta^{14}\text{CO}_2$  measurements that was remediated during the year.

453 **Table 2: Annual mean  $\Delta^{14}\text{CO}_2$  (in units of ‰) with standard deviations at JFJ from this study and from ICOS**

454 **(Emmenegger et al., 2025a). The numbers in brackets represent the number of values per year considered for the annual**

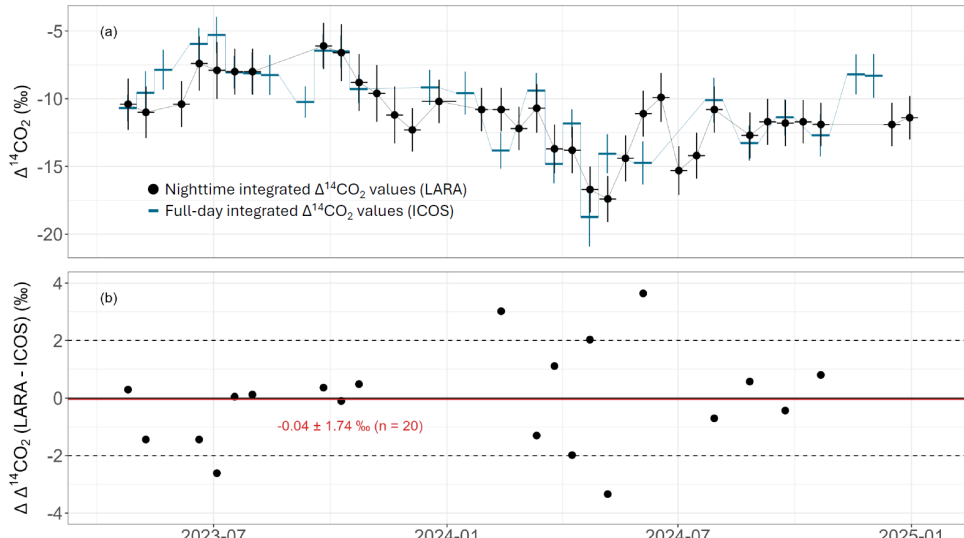
455 **mean.**



	2019	2020	2021	2022	2023	2024
This study	$-2.0 \pm 3.8$ (n = 17)	$-1.7 \pm 2.3$ (n = 15)	$-3.6 \pm 2.6$ (n = 25)	$-4.8 \pm 2.1$ (n = 22)	$-8.0 \pm 2.3$ (n = 21)	$-12.6 \pm 2.0$ (n = 21)
ICOS	$1.6 \pm 2.2$ (n = 15)	$-0.7 \pm 3.4$ (n = 14)	$-5.0 \pm 2.5$ (n = 21)	$-5.0 \pm 2.5$ (n = 19)	$-7.5 \pm 2.1$ (n = 18)	$-12.2 \pm 3.0$ (n = 14)

457

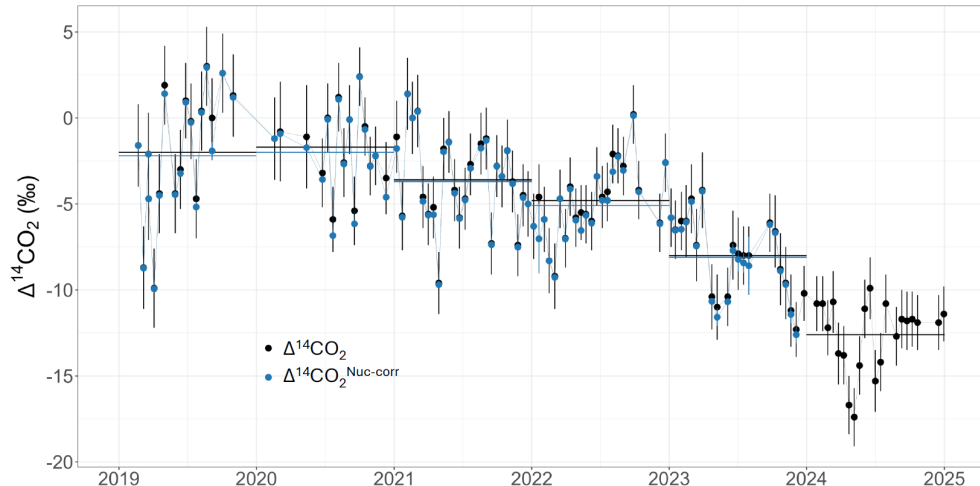
458 After the JASS installation in 2023, a more detailed comparison of  $\Delta^{14}\text{CO}_2$  with ICOS became possible, as we use  
 459 the same 14-day sampling as the ICOS integrated sodium hydroxide solution sampling (Fig. 6). Over about 20  
 460 months the mean difference was  $-0.04 \pm 1.74 \text{‰}$  (n = 20) with (insignificantly) lower values in our data. A few  
 461 large differences up to  $\pm 4 \text{‰}$  were observed. We emphasize that even though the biweekly periods are the same,  
 462 our JASS sampler integrates only nighttime hours whereas the ICOS sampler integrates all day; moreover, the air  
 463 inlet of our system is situated about 3 m higher than the one from the ICOS sampler. Therefore, the measurements  
 464 are not conducted on the exact same air. However, the insignificant mean difference suggests that the different  
 465 sampling conditions affect the measured  $\Delta^{14}\text{CO}_2$  only marginally.



466

467 **Figure 6:** (a) comparison between nighttime-integrated  $\Delta^{14}\text{CO}_2$  values from our LARA program (black points) and all-  
 468 day-integrated  $\Delta^{14}\text{CO}_2$  values from the ICOS program (blue lines). (b) Difference between LARA and ICOS of  $\Delta^{14}\text{CO}_2$   
 469 values for simultaneous samples. The solid black line represents the zero line and the typical  $\Delta^{14}\text{CO}_2$  measurement  
 470 uncertainty of  $\pm 2 \text{‰}$  are shown as dotted black lines. The red line shows the mean difference between both datasets of  
 471  $-0.04 \pm 1.74 \text{‰}$  (n = 20).

472 Similar to the correction we made using the simulated  $^{14}\text{CH}_4$  nuclear influence on  $\Delta^{14}\text{CH}_4$  measurements, we also  
 473 make a correction using the simulated  $^{14}\text{CO}_2$  nuclear influence on  $\Delta^{14}\text{CO}_2$  measurements (Fig. 7). The mean  
 474 nuclear  $\Delta^{14}\text{CO}_2$  influence is  $0.2 \pm 0.4 \text{‰}$  (min = 0, max =  $2.3 \text{‰}$ ). The overall effect of nuclear  $^{14}\text{C}$  emissions on  
 475 atmospheric  $\Delta^{14}\text{CO}_2$  is less than for  $\Delta^{14}\text{CH}_4$ , *i.e.*,  $0.2 \pm 0.4 \text{‰}$  compared to  $7 \pm 9 \text{‰}$ , respectively. Moreover,  
 476 nuclear  $^{14}\text{CO}_2$  emissions (from BWRs and NFRP) are known to be less sporadic than  $^{14}\text{CH}_4$  emissions from PWR  
 477 reactors (Stenström et al., 1995b), so our atmospheric model based on monthly nuclear  $^{14}\text{C}$  releases simulates  
 478 better nuclear  $^{14}\text{CO}_2$  contributions than  $^{14}\text{CH}_4$  contributions.



479

480 Figure 7: Raw  $\Delta^{14}\text{CO}_2$  values measured at JFJ (black points) and corresponding nuclear-corrected  $\Delta^{14}\text{CO}_2^{\text{Nuc-corr}}$  values  
481 from which the mean nuclear influence was subtracted (blue points). The vertical blue bar around each blue point  
482 corresponds to the standard deviation of the nuclear influence over the sampling period. Annual horizontal black lines  
483 correspond to the annual mean raw  $\Delta^{14}\text{CO}_2$  value derived from the black points. Annual horizontal blue lines  
484 correspond to the annual mean  $\Delta^{14}\text{CO}_2^{\text{Nuc-corr}}$  value derived from the blue points. Simulations for 2024 have not been  
485 available yet due to missing input parameters for this year.

486

#### 4. Discussion

487 Our  $\Delta^{14}\text{CH}_4$  measurements at JFJ represent the first direct multi-annual time-series of atmospheric measurements  
488 in the Northern Hemisphere published within the last 25 years. By the introduction of integrated nighttime  
489 sampling, Rn data-based filtering and correction of the nuclear influence, we have generated a representative multi-  
490 annual dataset of Northern midlatitude background air available with the reported  $\Delta^{14}\text{CH}_4^{\text{Rn-filt} + \text{Nuc-corr}}$  data. As the  
491 measurements at JFJ are consistent with previous measurements and global model simulations, continued  
492 observations at JFJ will provide an important constraint on the global background  $\Delta^{14}\text{CH}_4$  trends and the global  
493  $\text{CH}_4$  budget (Fujita et al. 2025).

494 The correction for the NPP influence on  $\Delta^{14}\text{CH}_4$  that we apply to the measurements may even be improved with  
495 more information on regional nuclear  $^{14}\text{C}$  emissions. Our current atmospheric simulation uses monthly constant  
496  $^{14}\text{CH}_4$  emission rates to describe the NPP releases in Switzerland and less frequent data for reactors in other  
497 countries. However, it is known that radioactive emissions from PWRs are rather sporadic (Stenström et al.,  
498 1995b). Espic et al. (2025) collected air samples for atmospheric  $^{14}\text{CH}_4$  and  $^{14}\text{CO}_2$  analyses around the Swiss PWR  
499 Gösgen during its annual revision period in 2019 and observed a  $^{14}\text{CH}_4$  and  $^{14}\text{CO}_2$  release event that lasted only a  
500 few hours but included  $\sim 8\%$  of the total annual  $^{14}\text{CH}_4$  emissions of that year. They found that the activities of noble  
501 gases measured at a 10-min temporal resolution at the PWR stack may be a valuable proxy to identify sporadic  
502  $^{14}\text{C}$  releases. A generalized use of this kind of high-frequency data would be beneficial to refine temporal variation  
503 in estimates of  $^{14}\text{C}$  emissions from NPPs.

504 The composition of  $^{14}\text{C}$  is another important uncertainty for estimates of  $^{14}\text{C}$  emissions from NPPs. Here, only  
505 PWRs and VVERs were considered to emit organic  $^{14}\text{C}$  (e.g.,  $^{14}\text{CH}_4$ ); however, small organic  $^{14}\text{C}$  emissions have  
506 also been reported for other reactor types: up to 7 % for BWRs (Kunz, 1985; Stenström et al., 1995a), 1-4 to 25-  
507 30 % for PHWRs (Bharath et al., 2022; IAEA, 2004; Joshi et al., 1987; Milton et al., 1995), and up to 30 % for  
508 LWGRs (Gaiko et al., 1985; Konstantinov et al., 1989). Organic  $^{14}\text{C}$  emissions from these reactor types may be  
509 significant as about 13 % of the total nuclear electricity is produced by BWRs (which is the third-most important  
510 reactor type after PWRs and VVERs based on nuclear electricity) and the emission factors for PHWRs and LWGRs  
511 (1.6 and 1.3 TBq/GWa, respectively, Zazzeri et al. (2018)) are even several times higher than for PWRs and  
512 VVERs. LWGR emissions are particularly uncertain, and radiocarbon measurements of tree rings around LWGRs  
513 suggested emission factors could be two to four times higher than the assumed value of 1.3 TBq/GWa (Juodis et  
514 al., 2022; Nazarov et al., 2023). In addition, PWRs themselves exhibit a broad range (*i.e.*, 44-95 %) for the organic



515  $^{14}\text{C}$  fraction at PWRs and VVERs. Furthermore, there are only few 40-year old measurements of the speciation of  
516 the individual fractions of the organic  $^{14}\text{C}$  emissions that may involve (besides  $^{14}\text{CH}_4$ ) relevant portions of *e.g.*  
517  $^{14}\text{C}_2\text{H}_6$ ,  $^{14}\text{C}_3\text{H}_8$  and  $^{14}\text{C}_4\text{H}_{10}$  (Kunz, 1985). More recently, Espic et al. (2025) found for the Swiss PWR Gösgen (see  
518 above) that the measured ratio between  $^{14}\text{CH}_4$  and  $^{14}\text{CO}_2$  emissions and the reported ratio between organic and  
519  $^{14}\text{CO}_2$  emissions agreed with each other, implying that almost all the organic emissions are in form of  $^{14}\text{CH}_4$ . More  
520 measurements focusing on the hydrocarbon composition of the organic  $^{14}\text{C}$  fraction are needed at PWRs, VVERs  
521 and LWGRs.

522 This work demonstrates that our measurements of  $\Delta^{14}\text{CO}_2$  at JFJ are generally consistent with concurrent  
523 measurements from the ICOS program. The installation of the JASS system in 2023 furthermore constitutes an  
524 improvement of the long-running ICOS  $\Delta^{14}\text{CO}_2$  measurements at JFJ, since it integrates nighttime periods which  
525 mostly are dominated by air from the free troposphere, whereas the ICOS measurements rely on all-day air  
526 sampling. Even though the insignificantly low mean  $\Delta\Delta^{14}\text{CO}_2$  suggests that the different sampling conditions affect  
527 the measured  $\Delta^{14}\text{CO}_2$  only marginally (Fig. 6), this observation requires a longer duration for the comparison of  
528 both datasets to prove their consistency.

529

## 530 **5. Conclusions**

531 We conducted biweekly atmospheric  $\Delta^{14}\text{CH}_4$  and  $\Delta^{14}\text{CO}_2$  measurements at the Swiss High-Altitude Research  
532 Station Jungfraujoch (about 3500 m a.s.l.) between 2019 and 2024. Initially based on 20–60-minute air samples  
533 commonly collected in the early morning, a novel air sampling setup automatically collecting ambient air during  
534 nighttime was installed in April 2023. Over the six years 2019–2024,  $\Delta^{14}\text{CH}_4$  values at JFJ have shown a slight  
535 increase from  $350 \pm 19\text{‰}$  to  $381 \pm 13\text{‰}$  (*i.e.*, by a rate of  $\sim+6\text{‰/yr}$ ) while  $\Delta^{14}\text{CO}_2$  values decreased from  
536  $-2.0 \pm 3.8\text{‰}$  to  $-12.6 \pm 2.0\text{‰}$  (*i.e.*, by a rate of  $\sim-2\text{‰/yr}$ ). Our  $\Delta^{14}\text{CO}_2$  values generally agree well with the  
537 integrated  $\Delta^{14}\text{CO}_2$  measurements from the ICOS program. Accounting for nuclear  $^{14}\text{CH}_4$  and  $^{14}\text{CO}_2$  emissions on  
538 the European scale within the atmospheric transport model FLEXPART-COSMO, we simulate the nuclear signal  
539 on our individual measurements at JFJ and estimate an average nuclear influence of  $7 \pm 9\text{‰}$  and  $0.2 \pm 0.4\text{‰}$  for  
540  $\Delta^{14}\text{CH}_4$  and  $\Delta^{14}\text{CO}_2$ , respectively, which we use to correct the observed data. Our  $\Delta^{14}\text{CH}_4$  data are consistent with  
541 an atmospheric one-box model for  $\Delta^{14}\text{CH}_4$  that simulates slightly increasing or decreasing  $\Delta^{14}\text{CH}_4$  over 2013–2024,  
542 depending on the strength of nuclear power plant emissions. Our new observations at JFJ will help to refine the  
543 global background  $\Delta^{14}\text{CH}_4$  and  $\Delta^{14}\text{CO}_2$  and to constrain  $\text{CH}_4$  and  $\text{CO}_2$  sources and sinks.

## 544 **Data availability**

545 All raw values presented in this work will be made available after publication on Zenodo.

## 546 **Author contributions**

547 **TL:** Conceptualization, Data curation, Formal analysis, Investigation, Methodology, Project administration,  
548 Software, Validation, Visualization, Writing – original draft, Writing – review and editing. **DG:** Data curation,  
549 Investigation Methodology, Validation, Visualization, Writing – original draft, Writing – review and editing. **SH:**  
550 Investigation Methodology, Software, Validation, Visualization, Writing – original draft, Writing – review and  
551 editing. **RF:** Investigation Methodology, Software, Validation, Visualization, Writing – original draft, Writing –  
552 review and editing. **HG:** Supervision, Writing – original draft, Writing – review and editing. **CE:** Data curation,  
553 Writing – review and editing. **MB:** Data curation, Writing – review and editing. **NH:** Investigation, Writing –  
554 review and editing. **FC:** Investigation, Writing – review and editing. **DB:** Investigation, Writing – review and  
555 editing. **MS:** Investigation, Writing – review and editing. **GZ:** Investigation, Writing – review and editing. **SH:**  
556 Investigation, Writing – review and editing. **ML:** Investigation, Writing – review and editing. **SS:**  
557 Conceptualization, Funding acquisition, Project administration, Resources, Supervision, Writing – review and  
558 editing.



559 **Competing interests**

560 The authors declare that they have no conflict of interest.

561

562 **Acknowledgements**

563 We are grateful to the funding of the SNSF Sinergia funding n°193770 (Radiocarbon Inventories of Switzerland –  
564 RICH: integrated approach to understand the changing carbon cycle) as well as the Dr. Alfred Bretscher  
565 Scholarship. We thank Gary Salazar, Franziska Lechleitner and Tiberiu Sava for their assistance during  $^{14}\text{C}$   
566 measurements at LARA. We further thank the operating company of the Paks nuclear power plant (MVM Paks  
567 Nuclear Power Plant Ltd.) for sharing the corresponding  $^{14}\text{C}$  emission values and Mihály Molnár for ensuring the  
568 communication with it. We are grateful to the team of the DCBP workshop (especially Sandra Hostettler and  
569 Thomas Hübscher) as well as René Schraner for their assistance in designing and building the JASS. We also thank  
570 the International Foundation High-Altitude Research Stations Jungfraujoch and Gornergrat for access to  
571 Jungfraujoch facilities and the Jungfraujoch's custodians (Joan & Martin Fischer, Christine & Ruedi Käser,  
572 Daniela Bissig & Erich Furrer, and Sonja Stöckli & Thomas Furter) for their support on site. We are grateful to  
573 Scott Chambers and his colleagues at Australian Nuclear Science and Technology Organisation (ANSTO) for the  
574 ongoing collaboration and support in maintaining the radon detection system. The radon and greenhouse gas  
575 concentration observations were financially supported by the Swiss National Science Foundation (SNSF,  
576 20FI20\_173691, 20FI20\_198227, 20FI-0\_229655) as a contribution to the pan-European Integrated Carbon  
577 Observation System (ICOS) Research Infrastructure. We thank ICOS for making available a large number of  
578 parameters continuously measured at JFJ. We thank the Global Monitoring Laboratory (GML) of the US National  
579 Oceanic & Atmospheric Administration (NOAA) for making available global  $\text{CH}_4$  and  $\text{CO}_2$  atmospheric levels.  
580 We finally thank Lukas Bäni, René Bleisch and Rolf Bütkofer for their assistance in configuring the remote  
581 access of the JASS.



582 **References**

583 Basu, S., Lehman, S. J., Miller, J. B., Andrews, A. E., Sweeney, C., Gurney, K. R., Xu, X., Southon, J., and Tans,  
584 P. P.: Estimating US fossil fuel CO<sub>2</sub> emissions from measurements of <sup>14</sup>C in atmospheric CO<sub>2</sub>, Proc. Natl. Acad.  
585 Sci. U.S.A., 117, 13300–13307, <https://doi.org/10.1073/pnas.1919032117>, 2020.

586 Berhanu, T. A., Szidat, S., Brunner, D., Satar, E., Schanda, R., Nyfeler, P., Battaglia, M., Steinbacher, M.,  
587 Hammer, S., and Leuenberger, M.: Estimation of the fossil fuel component in atmospheric CO<sub>2</sub> based on  
588 radiocarbon measurements at the Beromünster tall tower, Switzerland, Atmospheric Chemistry and Physics, 17,  
589 <https://doi.org/10.5194/acp-17-10753-2017>, 2017.

590 Bharath, Arya Krishnan, K., D’Souza, R. S., Rashmi Nayak, S., Dileep, B. N., Ravi, P. M., Mangavi, S. S.,  
591 Salunke, G. S., Veerendra, D., and Karunakara, N.: Carbon-14 emission from the pressurized heavy water reactor  
592 nuclear power plant at Kaiga, India, Journal of Environmental Radioactivity, 255, 107006,  
593 <https://doi.org/10.1016/j.jenvrad.2022.107006>, 2022.

594 Conen, F.: Radon Monitors Jungfraujoch & Uni Bern Near Realtime Data - <https://sievju.org/pl/radon.pl>, 2025.

595 Conen, F. and Zimmermann, L.: Separating “free tropospheric conditions” from those “influenced by the  
596 planetary boundary layer” - [https://www.hfsjg.ch/reports/2020/pdf/120\\_UniBasel\\_Conen\\_radon\\_cf.pdf](https://www.hfsjg.ch/reports/2020/pdf/120_UniBasel_Conen_radon_cf.pdf),  
597 International Foundation HFSJG, 2020.

598 Ehhalt, D. H.: The atmospheric cycle of methane, Tellus, 26, 58–70, <https://doi.org/10.1111/j.2153-3490.1974.tb01952.x>, 1974.

600 Eisma, R., Borg, K. van der, Jong, A. F. M. de, Kieskamp, W. M., and Veltkamp, A. C.: Measurements of the <sup>14</sup>C  
601 content of atmospheric methane in The Netherlands to determine the regional emissions of <sup>14</sup>CH<sub>4</sub>, Nuclear Inst.  
602 and Methods in Physics Research, B, 92, [https://doi.org/10.1016/0168-583X\(94\)96044-5](https://doi.org/10.1016/0168-583X(94)96044-5), 1994.

603 Eisma, R., Vermeulen, A. T., and Borg, K. V. D.: <sup>14</sup>CH<sub>4</sub> emissions from nuclear power plants in northwestern  
604 Europe, Radiocarbon, 37, <https://doi.org/10.1017/S0033822200030952>, 1995.

605 Emmenegger, L., Leuenberger, M., and Steinbacher, M.: ICOS ATC <sup>14</sup>C Release analysed by ICOS CRL from  
606 Jungfraujoch (6.0 m), 2015-09-21–2024-11-25, ICOS RI,  
607 <https://hdl.handle.net/11676/AtmTz0bjTlwKST7jLLrHSHh>, 2025a.

608 Emmenegger, L., Harris, E., Leuenberger, M., and Steinbacher, M.: ICOS ATC CH<sub>4</sub> Release from Jungfraujoch  
609 (13.9 m), 2016-12-12–2025-03-31, ICOS RI, [https://hdl.handle.net/11676/\\_qRWgJ01HGIxRzpTZjGCWWJF](https://hdl.handle.net/11676/_qRWgJ01HGIxRzpTZjGCWWJF),  
610 2025b.

611 Emmenegger, L., Harris, E., Leuenberger, M., and Steinbacher, M.: ICOS ATC CO<sub>2</sub> Release from Jungfraujoch  
612 (13.9 m), 2016-12-12–2025-03-31, ICOS RI, <https://hdl.handle.net/11676/4ba-uo4FsoZbxFyfj0S6CaUQ>, 2025c.

613 Emmenegger, L., Harris, E., Leuenberger, M., Steinbacher, M., and Roulet, Y.-A.: ICOS ATC Meteo Release  
614 from Jungfraujoch (1.0 m), 2016-12-12–2025-03-31, ICOS RI,  
615 <https://hdl.handle.net/11676/6XYZaZIL0CPWhQmPTAY-Swghh>, 2025d.

616 Espic, C., Liechti, M., Battaglia, M., Paul, D., Röckmann, T., and Szidat, S.: Compound-Specific Radiocarbon  
617 Analysis of Atmospheric Methane: A New Preconcentration and Purification Setup, Radiocarbon, 61, 1461–  
618 1476, <https://doi.org/10.1017/RDC.2019.76>, 2019.

619 Espic, C., Laemmeli, T., Henne, S., Purtschert, R., and Szidat, S.: Atmospheric <sup>14</sup>CH<sub>4</sub>, <sup>14</sup>CO<sub>2</sub> and <sup>37</sup>Ar  
620 measurements around a Swiss pressurized water reactor during an annual revision period, Journal of  
621 Environmental Radioactivity, 281, 107576, <https://doi.org/10.1016/j.jenvrad.2024.107576>, 2025.

622 Etheridge, D. M., Steele, L. P., Langenfelds, R. L., Francey, R. J., Barnola, J. -M., and Morgan, V. I.: Natural and  
623 anthropogenic changes in atmospheric CO<sub>2</sub> over the last 1000 years from air in Antarctic ice and firn, J.  
624 Geophys. Res., 101, 4115–4128, <https://doi.org/10.1029/95JD03410>, 1996.

625 Etiope, G., Ciotoli, G., Benà, E., Mazzoli, C., Röckmann, T., Sivan, M., Squartini, A., Laemmeli, T., Szidat, S.,  
626 Haghipour, N., and Sassi, R.: Surprising concentrations of hydrogen and non-geological methane and carbon



627 dioxide in the soil, *Science of The Total Environment*, 948, 174890,  
628 <https://doi.org/10.1016/j.scitotenv.2024.174890>, 2024.

629 European Commission. Joint Research Centre.: GHG emissions of all world countries: 2023., Publications  
630 Office, LU, 2023.

631 Fujita, R., Graven, H., Zazzeri, G., Hmiel, B., Petrenko, V. V., Smith, A. M., Michel, S. E., and Morimoto, S.:  
632 Global fossil methane emissions constrained by multi-isotopic atmospheric methane histories, *JGR-Atmospheres*, <https://doi.org/10.1029/2024JD041266>, 2025.

633 Gaiko, V. B., Koralev, N. A., Solov'ev, E. N., Trosheva, T. I., Shamov, V. P., Umanets, M. P., and Shcherbina, V. G.: Discharge of  $^{14}\text{C}$  by nuclear power stations with RBMK-1000 reactors, *At Energy*, 59, 703–705,  
634 <https://doi.org/10.1007/BF01122497>, 1985.

635 Gidden, M. J., Riahi, K., Smith, S. J., Fujimori, S., Luderer, G., Kriegler, E., Van Vuuren, D. P., Van Den Berg, M., Feng, L., Klein, D., Calvin, K., Doelman, J. C., Frank, S., Fricko, O., Harmsen, M., Hasegawa, T., Havlik, P., Hilaire, J., Hoesly, R., Horing, J., Popp, A., Stehfest, E., and Takahashi, K.: Global emissions pathways under  
636 different socioeconomic scenarios for use in CMIP6: a dataset of harmonized emissions trajectories through the end of the century, *Geosci. Model Dev.*, 12, 1443–1475, <https://doi.org/10.5194/gmd-12-1443-2019>, 2019.

637 Gonzalez Moguel, R., Vogel, F., Ars, S., Schaefer, H., Turnbull, J. C., and Douglas, P. M. J.: Using carbon-14 and carbon-13 measurements for source attribution of atmospheric methane in the Athabasca oil sands region, *Atmos. Chem. Phys.*, 22, 2121–2133, <https://doi.org/10.5194/acp-22-2121-2022>, 2022.

638 Graven, H., Fischer, M. L., Lueker, T., Jeong, S., Guilderson, T. P., Keeling, R. F., Bambha, R., Brophy, K.,  
639 Callahan, W., Cui, X., Frankenberg, C., Gurney, K. R., LaFranchi, B. W., Lehman, S. J., Michelsen, H., Miller, J.,  
640 Newman, S., Paplawsky, W., Parazoo, N. C., Sloop, C., and Walker, S. J.: Assessing fossil fuel  $\text{CO}_2$  emissions  
641 in California using atmospheric observations and models, *Environ. Res. Lett.*, 13, 065007,  
642 <https://doi.org/10.1088/1748-9326/aabd43>, 2018.

643 Graven, H., Hocking, T., and Zazzeri, G.: Detection of Fossil and Biogenic Methane at Regional Scales Using  
644 Atmospheric Radiocarbon, *Earth's Future*, 7, 283–299, <https://doi.org/10.1029/2018EF001064>, 2019.

645 Graven, H., Keeling, R. F., and Rogelj, J.: Changes to Carbon Isotopes in Atmospheric  $\text{CO}_2$  Over the Industrial  
646 Era and Into the Future, *Global Biogeochemical Cycles*, 34, e2019GB006170,  
647 <https://doi.org/10.1029/2019GB006170>, 2020.

648 Griffiths, A. D., Conen, F., Weingartner, E., Zimmermann, L., Chambers, S. D., Williams, A. G., and  
649 Steinbacher, M.: Surface-to-mountaintop transport characterised by radon observations at the Jungfraujoch,  
650 *Atmos. Chem. Phys.*, 14, 12763–12779, <https://doi.org/10.5194/acp-14-12763-2014>, 2014.

651 Hammer, S., Friedrich, R., Kromer, B., Cherkinsky, A., Lehman, S. J., Meijer, H. A. J., Nakamura, T., Palonen, V., Reimer, R. W., Smith, A. M., Southon, J. R., Szidat, S., Turnbull, J., and Uchida, M.: Compatibility of  
652 Atmospheric  $^{14}\text{CO}_2$  Measurements: Comparing the Heidelberg Low-Level Counting Facility to International  
653 Accelerator Mass Spectrometry (AMS) Laboratories, *Radiocarbon*, 59, 875–883,  
654 <https://doi.org/10.1017/RDC.2016.62>, 2017.

655 Heiskanen, J., Brümmer, C., Buchmann, N., Calfapietra, C., Chen, H., Gielen, B., Gkritzalis, T., Hammer, S.,  
656 Hartman, S., Herbst, M., Janssens, I. A., Jordan, A., Juurola, E., Karstens, U., Kasurinen, V., Kruijt, B.,  
657 Lankreijer, H., Levin, I., Linderson, M.-L., Loustau, D., Merbold, L., Myhre, C. L., Papale, D., Pavelka, M.,  
658 Pilegaard, K., Ramonet, M., Rebmann, C., Rinne, J., Rivier, L., Saltikoff, E., Sanders, R., Steinbacher, M.,  
659 Steinhoff, T., Watson, A., Vermeulen, A. T., Vesala, T., Vítková, G., and Kutsch, W.: The Integrated Carbon  
660 Observation System in Europe, *Bulletin of the American Meteorological Society*, 103, E855–E872,  
661 <https://doi.org/10.1175/BAMS-D-19-0364.1>, 2022.

662 Henne, S., Brunner, D., Folini, D., Solberg, S., Klausen, J., and Buchmann, B.: Assessment of parameters  
663 describing representativeness of air quality in-situ measurement sites, *Atmos. Chem. Phys.*, 10, 3561–3581,  
664 <https://doi.org/10.5194/acp-10-3561-2010>, 2010.



673 Henne, S., Brunner, D., Oney, B., Leuenberger, M., Eugster, W., Bamberger, I., Meinhardt, F., Steinbacher, M.,  
674 and Emmenegger, L.: Validation of the Swiss methane emission inventory by atmospheric observations and  
675 inverse modelling, *Atmos. Chem. Phys.*, 16, 3683–3710, <https://doi.org/10.5194/acp-16-3683-2016>, 2016.

676 Hmiel, B., Petrenko, V. V., Dyonisius, M. N., Buzert, C., Smith, A. M., Place, P. F., Harth, C., Beaudette, R.,  
677 Hua, Q., Yang, B., Vimont, I., Michel, S. E., Severinghaus, J. P., Etheridge, D., Bromley, T., Schmitt, J., Fain, X.,  
678 Weiss, R. F., and Dlugokencky, E.: Preindustrial  $^{14}\text{CH}_4$  indicates greater anthropogenic fossil  $\text{CH}_4$  emissions,  
679 *Nature*, 578, 409–412, <https://doi.org/10.1038/s41586-020-1991-8>, 2020.

680 IAEA: Management of Waste Containing Tritium and Carbon-14, Technical Reports Series, 421, 2004.

681 IAEA PRIS: World Statistics, <https://pris.iaea.org/PRIS/WorldStatistics/OperationalReactorsByType.aspx>, 2025.

682 IPCC: Climate Change 2021 – The Physical Science Basis: Working Group I Contribution to the Sixth  
683 Assessment Report of the Intergovernmental Panel on Climate Change, 1st ed., Cambridge University Press,  
684 <https://doi.org/10.1017/9781009157896>, 2023.

685 Joshi, M. L., Ramamirtham, B., and Soman, S. D.: Measurement of  $^{14}\text{C}$  Emission Rates From a Pressurised  
686 Heavy Water Reactor, *Health Physics*, 52, 787–791, <https://doi.org/10.1097/00004032-198706000-00009>, 1987.

687 Juodis, L., Maceika, E., Barisevičiūtė, R., Pabedinskas, A., Ežerinskis, Ž., Šapolaitė, J., Plukis, A., and Remeikis,  
688 V.: Radiocarbon generation and atmospheric release assessment from nuclear power plant with RBMK type  
689 reactors, *Nuclear Engineering and Design*, 394, 111822, <https://doi.org/10.1016/j.nucengdes.2022.111822>, 2022.

690 Katharopoulos, I., Rust, D., Vollmer, M. K., Brunner, D., Reimann, S., O'Doherty, S. J., Young, D., Stanley, K.  
691 M., Schuck, T., Arduini, J., Emmenegger, L., and Henne, S.: Impact of transport model resolution and a priori  
692 assumptions on inverse modeling of Swiss F-gas emissions, *Atmos. Chem. Phys.*, 23, 14159–14186,  
693 <https://doi.org/10.5194/acp-23-14159-2023>, 2023.

694 Konstantinov, E. A., Korablev, N. A., Solov'ev, E. N., Shamov, V. P., Fedorov, V. L., and Litvinov, A. M.:  $^{14}\text{C}$   
695 emission from RBMK-1500 reactors and features determining it, *At Energy*, 66, 77–79,  
696 <https://doi.org/10.1007/BF01121081>, 1989.

697 Kunz, C.: Carbon-14 Discharge at Three Light-water Reactors, *Health Physics*, 49, 25–35,  
698 <https://doi.org/10.1097/00004032-198507000-00002>, 1985.

699 Kutschera, W.: The Half-Life of  $^{14}\text{C}$ —Why Is It So Long?, *Radiocarbon*, 61, 1135–1142,  
700 <https://doi.org/10.1017/RDC.2019.26>, 2019.

701 Laemmel, T. and Szidat, S.: Compilation of annual nuclear electricity production per reactor from 1954 to 2023,  
702 <https://doi.org/10.5281/ZENODO.14535156>, 2025.

703 Laemmel, T., Knaack, T., Heckel, A., Wenger, A., and Szidat, S.: Compilation of nuclear industry's gaseous  
704 radiocarbon emissions from 1950 to 2023, <https://doi.org/10.5281/ZENODO.15034662>, 2025.

705 Lan, X., Thoning, K., and Dlugokencky, E.: Trends in globally-averaged  $\text{CH}_4$ ,  $\text{N}_2\text{O}$ , and  $\text{SF}_6$  determined from  
706 NOAA Global Monitoring Laboratory measurements. Version 2025-08 (2025-08),  
707 <https://doi.org/10.15138/P8XG-AA10>, 2025a.

708 Lan, X., Tans, P., and Thoning, K.: Trends in globally-averaged  $\text{CO}_2$  determined from NOAA Global Monitoring  
709 Laboratory measurements. Version 2025-08 (2025-08), <https://doi.org/10.15138/9N0H-ZH07>, 2025b.

710 Lassey, K. R., Etheridge, D. M., Lowe, D. C., Smith, A. M., and Ferretti, D. F.: Centennial evolution of the  
711 atmospheric methane budget: what do the carbon isotopes tell us?, *Atmospheric Chemistry and Physics*, 7, 2119–  
712 2139, <https://doi.org/10.5194/acp-7-2119-2007>, 2007a.

713 Lassey, K. R., Lowe, D. C., and Smith, A. M.: The atmospheric cycling of radiomethane and the “fossil fraction”  
714 of the methane source, *Atmospheric Chemistry and Physics*, 7, 2141–2149, <https://doi.org/10.5194/acp-7-2141-2007b>, 2007b.



716 Leuenberger, M. and Flückiger, E.: Research at Jungfraujoch, *Science of The Total Environment*, 391, 169–176,  
717 https://doi.org/10.1016/j.scitotenv.2007.10.044, 2008.

718 Levin, I. and Kromer, B.: The Tropospheric  $^{14}\text{CO}_2$  Level in Mid-Latitudes of the Northern Hemisphere (1959–  
719 2003), *Radiocarbon*, 46, 1261–1272, https://doi.org/10.1017/S0033822200033130, 2004.

720 Levin, I., Kromer, B., Schoch-Fischer, H., Bruns, M., Münnich, M., Berdau, D., Vogel, J. C., and Münnich, K.  
721 O.: 25 Years of Tropospheric  $^{14}\text{C}$  Observations in Central Europe, *Radiocarbon*, 27, 1–19,  
722 https://doi.org/10.1017/S0033822200006895, 1985.

723 Levin, I., Bösinger, R., Bonani, G., Francey, R. J., Kromer, B., Münnich, K. O., Suter, M., Trivett, N. B. A., and  
724 Wölfli, W.: Radiocarbon in Atmospheric Carbon Dioxide and Methane: Global Distribution and Trends, in:  
725 Radiocarbon After Four Decades, edited by: Taylor, R. E., Long, A., and Kra, R. S., Springer New York, New  
726 York, NY, 503–518, https://doi.org/10.1007/978-1-4757-4249-7\_31, 1992.

727 Levin, I., Kromer, B., Schmidt, M., and Sartorius, H.: A novel approach for independent budgeting of fossil fuel  
728  $\text{CO}_2$  over Europe by  $^{14}\text{CO}_2$  observations, *Geophysical Research Letters*, 30, 2003GL018477,  
729 https://doi.org/10.1029/2003GL018477, 2003.

730 Levin, I., Naegler, T., Kromer, B., Diehl, M., Francey, R. J., Gomez-Pelaez, A. J., Steele, L. P., Wagenbach, D.,  
731 Weller, R., and Worthy, D. E.: Observations and modelling of the global distribution and long-term trend of  
732 atmospheric  $^{14}\text{CO}_2$ , *Tellus B: Chemical and Physical Meteorology*, 62, 26, https://doi.org/10.1111/j.1600-  
733 0889.2009.00446.x, 2010.

734 Levin, I., Kromer, B., and Hammer, S.: Atmospheric  $\Delta^{14}\text{CO}_2$  trend in Western European background air from  
735 2000 to 2012, *Tellus B: Chemical and Physical Meteorology*, 65, 20092,  
736 https://doi.org/10.3402/tellusb.v65i0.20092, 2013.

737 Levin, I., Preunkert, S., Graven, H., Lewis, C., Miller, J. B., Turnbull, J. C., Xu, X., and Hammer, S.: Database of  
738 existing  $^{14}\text{CO}_2$  measurements - CO2MVS Research on Supplementary Observations (CORSO), European  
739 Union, 2023.

740 Lowe, D. C., Brenninkmeijer, C. A. M., Manning, M. R., Sparks, R., and Wallace, G.: Radiocarbon  
741 determination of atmospheric methane at Baring Head, New Zealand, *Nature*, 332, 522–525,  
742 https://doi.org/10.1038/332522a0, 1988.

743 Manning, M. R., Lowe, D. C., Melhuish, W. H., Sparks, R. J., Wallace, G., Brenninkmeijer, C. A. M., and  
744 McGill, R. C.: The Use of Radiocarbon Measurements in Atmospheric Studies, *Radiocarbon*, 32, 37–58,  
745 https://doi.org/10.1017/S0033822200039941, 1990.

746 Milton, G. M., Kramer, S. J., Brown, R. M., Repta, C. J. W., King, K. J., and Rao, R. R.: Radiocarbon Dispersion  
747 around Canadian Nuclear Facilities, *Radiocarbon*, 37, 485–496, https://doi.org/10.1017/S0033822200030964,  
748 1995.

749 Nazarov, E. I., Kruzhakov, A. V., Vasyanovich, M. E., Ekidin, A. A., Pyshkina, M. D., Kukarskikh, V. V., and  
750 Parkhomchuk, E. V.:  $^{14}\text{C}$  in tree rings in the vicinity of the RBMK reactor nuclear power plant, *Radiocarbon*, 65,  
751 1343–1350, https://doi.org/10.1017/RDC.2023.125, 2023.

752 Němec, M., Wacker, L., and Gäggeler, H.: Optimization of the Graphitization Process at Age-1, *Radiocarbon*, 52,  
753 1380–1393, https://doi.org/10.1017/S0033822200046464, 2010.

754 Nisbet, E. G., Manning, M. R., Dlugokencky, E. J., Michel, S. E., Lan, X., Röckmann, T., Denier Van Der Gon,  
755 H. A. C., Schmitt, J., Palmer, P. I., Dyonisius, M. N., Oh, Y., Fisher, R. E., Lowry, D., France, J. L., White, J. W.  
756 C., Brailsford, G., and Bromley, T.: Atmospheric Methane: Comparison Between Methane's Record in 2006–  
757 2022 and During Glacial Terminations, *Global Biogeochemical Cycles*, 37, e2023GB007875,  
758 https://doi.org/10.1029/2023GB007875, 2023.

759 Nydal, R. and Lövseth, K.: Tracing bomb  $^{14}\text{C}$  in the atmosphere 1962–1980, *J. Geophys. Res.*, 88, 3621–3642,  
760 https://doi.org/10.1029/JC088iC06p03621, 1983.



761 Pieber, S. M., Tuzson, B., Henne, S., Karstens, U., Gerbig, C., Koch, F.-T., Brunner, D., Steinbacher, M., and  
762 Emmenegger, L.: Analysis of regional CO<sub>2</sub> contributions at the high Alpine observatory Jungfraujoch by means  
763 of atmospheric transport simulations and  $\delta^{13}\text{C}$ , *Atmos. Chem. Phys.*, 22, 10721–10749,  
764 <https://doi.org/10.5194/acp-22-10721-2022>, 2022.

765 Pisso, I., Sollum, E., Grythe, H., Kristiansen, N. I., Cassiani, M., Eckhardt, S., Arnold, D., Morton, D.,  
766 Thompson, R. L., Groot Zwaaftink, C. D., Evangelou, N., Sodemann, H., Haimberger, L., Henne, S., Brunner,  
767 D., Burkhardt, J. F., Fouilloux, A., Brioude, J., Philipp, A., Seibert, P., and Stohl, A.: The Lagrangian particle  
768 dispersion model FLEXPART version 10.4, *Geosci. Model Dev.*, 12, 4955–4997, <https://doi.org/10.5194/gmd-12-4955-2019>, 2019.

770 Quay, P., Stutsman, J., Wilbur, D., Snover, A., Dlugokencky, E., and Brown, T.: The isotopic composition of  
771 atmospheric methane, *Global Biogeochemical Cycles*, 13, 445–461, <https://doi.org/10.1029/1998GB900006>,  
772 1999.

773 Ruff, M., Wacker, L., Gäggeler, H. W., Suter, M., Synal, H.-A., and Szidat, S.: A Gas Ion Source for Radiocarbon  
774 Measurements at 200 kV, *Radiocarbon*, 49, 307–314, <https://doi.org/10.1017/S003382200042235>, 2007.

775 Saunois, M., Martinez, A., Poulter, B., Zhang, Z., Raymond, P. A., Regnier, P., Canadell, J. G., Jackson, R. B.,  
776 Patra, P. K., Bousquet, P., Ciais, P., Dlugokencky, E. J., Lan, X., Allen, G. H., Bastviken, D., Beerling, D. J.,  
777 Belikov, D. A., Blake, D. R., Castaldi, S., Crippa, M., Deemer, B. R., Dennison, F., Etiope, G., Gedney, N.,  
778 Höglund-Isaksson, L., Holgerson, M. A., Hopcroft, P. O., Hugelius, G., Ito, A., Jain, A. K., Jamardanan, R.,  
779 Johnson, M. S., Kleinen, T., Krummel, P. B., Lauerwald, R., Li, T., Liu, X., McDonald, K. C., Melton, J. R.,  
780 Mühle, J., Müller, J., Murguia-Flores, F., Niwa, Y., Noce, S., Pan, S., Parker, R. J., Peng, C., Ramonet, M., Riley,  
781 W. J., Rocher-Ros, G., Rosentreter, J. A., Sasakawa, M., Segers, A., Smith, S. J., Stanley, E. H., Thanwerdas, J.,  
782 Tian, H., Tsuruta, A., Tubiello, F. N., Weber, T. S., Van Der Werf, G. R., Worthy, D. E. J., Xi, Y., Yoshida, Y.,  
783 Zhang, W., Zheng, B., Zhu, Q., Zhu, Q., and Zhuang, Q.: Global Methane Budget 2000–2020, *Earth Syst. Sci.*  
784 *Data*, 17, 1873–1958, <https://doi.org/10.5194/essd-17-1873-2025>, 2025.

785 Schraff, C., Reich, H., Rhodin, A., Schomburg, A., Stephan, K., Periñez, A., and Potthast, R.: Kilometre-scale  
786 ensemble data assimilation for the COSMO model (KENDA), *Quart J Royal Meteorol Soc*, 142, 1453–1472,  
787 <https://doi.org/10.1002/qj.2748>, 2016.

788 Sparrow, K. J., Kessler, J. D., Southon, J. R., Garcia-Tigreros, F., Schreiner, K. M., Ruppel, C. D., Miller, J. B.,  
789 Lehman, S. J., and Xu, X.: Limited contribution of ancient methane to surface waters of the U.S. Beaufort Sea  
790 shelf, *Sci. Adv.*, 4, eaao4842, <https://doi.org/10.1126/sciadv.aao4842>, 2018.

791 Stenström, K., Erlandsson, B., Hellborg, R., Wiebert, A., and Skog, G.:  $^{14}\text{CO}_2$  and total airborne  $^{14}\text{C}$  releases  
792 from a PWR and a BWR at Ringhals nuclear power plant measured with accelerator mass spectrometry, 1995a.

793 Stenström, K., Erlandsson, B., Hellborg, R., Wiebert, A., Skog, S., Vesanan, R., Alpsten, M., and Bjurman, B.: A  
794 one-year study of the total air-borne  $^{14}\text{C}$  effluents from two Swedish light-water reactors, one boiling water- and  
795 one pressurized water reactor, *Journal of Radioanalytical and Nuclear Chemistry Articles*, 198, 203–213,  
796 <https://doi.org/10.1007/BF02038258>, 1995b.

797 Stenström, K. E., Skog, G., Georgiadou, E., Genberg, J., and Johansson, A.: A guide to radiocarbon units and  
798 calculations, Lund University, Department of Physics, Division of Nuclear Physics, 2011.

799 Stuiver, M. and Polach, H. A.: Discussion Reporting of  $^{14}\text{C}$  Data, *Radiocarbon*, 19, 355–363,  
800 <https://doi.org/10.1017/S003382200003672>, 1977.

801 Synal, H.-A., Stocker, M., and Suter, M.: MICADAS: A new compact radiocarbon AMS system, *Nuclear*  
802 *Instruments and Methods in Physics Research Section B: Beam Interactions with Materials and Atoms*, 259, 7–  
803 13, <https://doi.org/10.1016/j.nimb.2007.01.138>, 2007.

804 Szidat, S.:  $^{14}\text{C}$  Research at the Laboratory for the Analysis of Radiocarbon with AMS (LARA), University of  
805 Bern, *Chimia*, 74, 1010, <https://doi.org/10.2533/chimia.2020.1010>, 2020.

806 Townsend-Small, A., Tyler, S. C., Pataki, D. E., Xu, X., and Christensen, L. E.: Isotopic measurements of  
807 atmospheric methane in Los Angeles, California, USA: Influence of “fugitive” fossil fuel emissions, *Journal of*  
808 *Geophysical Research: Atmospheres*, 117, n/a-n/a, <https://doi.org/10.1029/2011JD016826>, 2012.



809 Turnbull, J. C., Lehman, S. J., Miller, J. B., Sparks, R. J., Southon, J. R., and Tans, P. P.: A new high precision  
810  $^{14}\text{CO}_2$  time series for North American continental air, *J. Geophys. Res.*, 112, 2006JD008184,  
811 <https://doi.org/10.1029/2006JD008184>, 2007.

812 Vance, J. N., Cline, J. E., and Robertson, D. E.: Characterization of Carbon-14 generated by the Nuclear Power  
813 industry, EPRI, Electric Power Research Institute, Palo Alto, California, 1995.

814 Wacker, L., Christl, M., and Synal, H.-A.: Bats: A new tool for AMS data reduction, *Nuclear Instruments and*  
815 *Methods in Physics Research Section B: Beam Interactions with Materials and Atoms*, 268, 976–979,  
816 <https://doi.org/10.1016/j.nimb.2009.10.078>, 2010.

817 Wacker, L., Fahrni, S. M., Hajdas, I., Molnar, M., Synal, H.-A., Szidat, S., and Zhang, Y. L.: A versatile gas  
818 interface for routine radiocarbon analysis with a gas ion source, *Nuclear Instruments and Methods in Physics*  
819 *Research Section B: Beam Interactions with Materials and Atoms*, 294, 315–319,  
820 <https://doi.org/10.1016/j.nimb.2012.02.009>, 2013.

821 Wahlen, M., Tanaka, N., Henry, R., Deck, B., Zeglen, J., Vogel, J. S., Southon, J., Shemesh, A., Fairbanks, R.,  
822 and Broecker, W.: Carbon-14 in Methane Sources and in Atmospheric Methane: The Contribution from Fossil  
823 Carbon, *Science*, 245, 286–290, <https://doi.org/10.1126/science.245.4915.286>, 1989.

824 WMO: The State of Greenhouse Gases in the Atmosphere Based on Global Observations through 2024, WMO,  
825 Geneva, 2025.

826 Yver-Kwok, C., Philippon, C., Bergamaschi, P., Biermann, T., Calzolari, F., Chen, H., Conil, S., Cristofanelli, P.,  
827 Delmotte, M., Hatakka, J., Heliasz, M., Hermansen, O., Komíková, K., Kubistin, D., Kumps, N., Laurent, O.,  
828 Laurila, T., Lehner, I., Levula, J., Lindauer, M., Lopez, M., Mammarella, I., Manca, G., Marklund, P., Metzger,  
829 J.-M., Mölder, M., Platt, S. M., Ramonet, M., Rivier, L., Scheeren, B., Sha, M. K., Smith, P., Steinbacher, M.,  
830 Vítková, G., and Wyss, S.: Evaluation and optimization of ICOS atmosphere station data as part of the labeling  
831 process, *Atmos. Meas. Tech.*, 14, 89–116, <https://doi.org/10.5194/amt-14-89-2021>, 2021.

832 Zazzeri, G., Yeomans, E. A., and Graven, H. D.: Global and Regional Emissions of Radiocarbon from Nuclear  
833 Power Plants from 1972 to 2016, *Radiocarbon*, 60, 1067–1081, <https://doi.org/10.1017/RDC.2018.42>, 2018.

834 Zazzeri, G., Xu, X., and Graven, H.: Efficient Sampling of Atmospheric Methane for Radiocarbon Analysis and  
835 Quantification of Fossil Methane, *Environ. Sci. Technol.*, 55, 8535–8541,  
836 <https://doi.org/10.1016/acs.est.0c03300>, 2021.

837 Zazzeri, G., Graven, H., Xu, X., Saboya, E., Blyth, L., Manning, A. J., Chawner, H., Wu, D., and Hammer, S.:  
838 Radiocarbon Measurements Reveal Underestimated Fossil  $\text{CH}_4$  and  $\text{CO}_2$  Emissions in London, *Geophysical*  
839 *Research Letters*, 50, e2023GL103834, <https://doi.org/10.1029/2023GL103834>, 2023.

840 Zazzeri, G., Wacker, L., Haghipour, N., Gautschi, P., Laemmel, T., Szidat, S., and Graven, H.: A new portable  
841 sampler of atmospheric methane for radiocarbon measurements, *Atmos. Meas. Tech.*, 18, 319–325,  
842 <https://doi.org/10.5194/amt-18-319-2025>, 2025.

843